THESIS FOR THE DEGREE OF DOCTOR OF PHILOSOPHY

Conducting Foams and Fibres for Bulk Plastic Thermoelectrics

JASON RYAN

Department of Chemistry and Chemical Engineering
CHALMERS UNIVERSITY OF TECHNOLOGY
Göteborg, Sweden 2018

Conducting Foams and Fibres for Bulk Plastic Thermoelectrics

JASON RYAN

ISBN: 978-91-7597-753-9

Doktorsavhandlingar vid Chalmers tekniska högskola

Ny Serie Nr: 4434

ISSN: 0346-718X

Department of Chemistry and Chemical Engineering
Division of Applied Chemistry
Chalmers University of Technology
SE-412 96 Göteborg
Sweden

Phone: +46 (0)31 772 1000

Cover:
Merged image of: right, normal photo of authors arm, taken by the author; left, thermal image of authors arm, taken by Dr Anja Lund; and top, a schematic of a textile thermoelectric module powering a light bulb, drawn by Dr Lund.

Chalmers Reproservice
Göteborg, Sweden 2018

"Now this is not the end.
It is not even the beginning of the end.
But it is, perhaps, the end of the beginning."

- Sir Winston Churchill

10th November 1942

Conducting Foams and Fibres for Bulk Plastic Thermoelectrics

Jason Ryan
Department of Chemistry and Chemical Engineering
Chalmers University of Technology
SE-412 96 Göteborg, Sweden

ABSTRACT

The use of small portable electronics in society is constantly increasing, thus the demand for portable power sources also rises in turn. Portable electronic devices rely upon energy stored in batteries to power them, which in turn require regular access to power outlets to be recharged. The development of organic thermoelectric materials is one potential solution towards charging devices, such as sensors and ID tags, whilst the user is mobile.

This thesis discusses thermoelectrics in the context of organics, specifically the development of materials with bulk architectures, where conjugated polymers have been used to attain functioning conducting systems. We present conducting p-type silk and n-type polyester based yarns which could ultimately prove useful for drawing upon waste heat energy from the human body, for example in the form of clothing. Additionally, foams have been developed which offer low thermal conductivities, ease of doping and comparable thermoelectric performances c.f thick films considering the amount of material present. We have also demonstrated a nanocomposite system which can be switched from p-type to n-type when irradiated with UV light, which lends itself as an ink that allows for patterning during printing.

Textile devices have been fabricated based upon p-type silk yarn dyed with PEDOT:PSS, which were further enhanced with n-type polyester yarn coated with a carbon nanotube composite, to produce an *all-organic* device which produces promising results in terms of thermoelectric output, offering an exciting direction for the growing field of organic thermoelectrics.

Keywords: *thermoelectrics, organic thermoelectrics, conjugated polymers, renewable energy, polymer foams, conducting yarn, conducting fibres, electronic textiles, e-textiles, nanocomposites.*

NOMENCLATURE

Chemical abbreviations

A-DCV-DPPTT	aromatic- dicyanovinyl-dipyrrolo[3,4-c]pyrrole-1,4-diylidene)bis(thieno[3,2-b]thiophene
BCF	tris(pentafluorophenyl)borane
CNT(s)	carbon nanotube(s)
DDQ	2,3-Dichloro-5,6-dicyano-1,4-benzoquinone
DMSO	dimethyl sulfoxide
DWNT(s)	double walled carbon nanotube(s)
EG	ethylene glycol
F4TCNQ	2,3,5,6-Tetrafluoro-7,7,8,8-tetracyanoquinodimethane
$Fe(Tos)_3$	iron(III) p-toluenesulfonate
GOPS	(3-glycidyloxypropyl)trimethoxysilane
HCl	hydrochloric acid
IP-TT	poly(6,6,12,12-tetraoctyldiindeno[1,2-b:1,2-e]-pyrazine-co-2,5-thieno[3,2-b]thiophene)
MeOH	methanol
MWNT(s)	multi-walled nanotube(s)
nDMBI	4-(1,3-Dimethyl-2,3-dihydro-1H-benzoimidazol-2-yl)phenyl)dimethylamine
N-MWNT(s)	nitrogen doped multi-walled nanotube(s)
oDCB	ortho dichlorobenzene
P3HT	poly(3-hexylthiophene-2,5-diyl)

PA	polyamide
PAc	polyacetylene
PAN	polyacrylonitrile
PaNi	polyaniline
PBTTT	poly[2,5-bis(3-tetradecylthiophen-2-yl)thieno[3,2-b]thiophene]
PEDOT	poly(3,4-ethylenedioxythiophene)
PEDOT:PSS	poly(3,4-ethylenedioxythiophene) polystyrene sulfonate
PEDOT-S	poly(4-(2,3-dihydrothieno[3,4-b]-[1,4]dioxin-2-yl-methoxy)-1-butanesulfonic acid)
PEDOT:Tos	poly(3,4-ethylenedioxythiophene)-tosylate
PEG	poly(ethylene glycol)
PEI	polyethylenimine
PET	poly(ethylene terephthalate)
PP	polypropylene
PSS	poly(styrene sulfonate)
PVAc	poly(vinyl acetate)
PVP	polyvinylpyrrolidone
pVpY	poly(4-vinylpyridine)
SIS	poly(styrene-isoprene-styrene)
SWNT(s)	single-walled carbon nanotube(s)
TCPP	tris(chloroisopropyl)phosphate

Symbols and abbreviations

α	Seebeck coefficient
Δ_p	probing depth
ΔT	temperature difference
ΔV	voltage difference
$\varepsilon_{\text{break}}$	stress at break
κ	thermal conductivity
μ	charge carrier mobility
ρ	resistivity
ρ_{d}	density
σ	electrical conductivity
c	concentration
c^*	percolation (concentration)
c_{s}	p-type-n-type switching point concentration
C_p	specific heat capacity
D	thermal diffusivity
DSC	differential scanning calorimetry
eV	electron volts
F	thin film 4-point-probe correction factor
HOMO	highest occupied molecular orbital
I	current
L	lorenz number

LUMO	lowest unoccupied molecular orbital
n	charge carrier concentration
$N_{element}$	number of elements
NP’s	nanoparticles
p	porosity
PF	power factor
P_{max}	maximum power
PL	photoluminescence
R	resistance
R_{int}	internal resistance
R_{load}	load resistance
r_s	sheet resistance
T	temperature
T_g	glass transition temperature
TIPS	thermally induced phase separation
SEM	scanning electron microscopy
UV	ultraviolet
V_p	pore volume fraction
V_{oc}	open circuit voltage
ZT	figure of merit
ZT'	volume adjusted ZT

PUBLICATIONS

This thesis consists of an extended summary and the following appended papers:

Paper I **Bulk Doping of Millimeter-Thick Conjugated Polymer Foams for Plastic Thermoelectrics**

Renee Kroon, Jason D. Ryan, David Kiefer, Liyang Yu, Jonna Hynynen, Eva Olsson, and Christian Müller

Advanced Functional Materials, 27 (2017), 1704183

Paper II **Photoinduced p- to n-type Switching in Thermoelectric Polymer-Carbon Nanotube Composites**

Bernhard Dörling, Jason D. Ryan, John D. Craddock, Andrea Sorrentino, Ahmed El Basaty, Andrés Gomez, Miquel Garriga, Eva Pereiro, John E. Anthony, Matthew C. Weisenberger, Alejandro R. Goñi, Christian Müller, and Mariano Campoy-Quiles

Advanced Materials, 28 (2016), 2782-2789

Paper III **Machine-Washable PEDOT:PSS Dyed Silk Yarns for Electronic Textiles**

Jason D. Ryan, Desalegn Alemu Mengistie, Roger Gabrielsson, Anja Lund, and Christian Müller

ACS Applied Materials and Interfaces, 9 (2017), 9045-9050

Paper IV **All-organic textile thermoelectrics with carbon nanotube coated n-type yarns**

Jason D. Ryan, Anja Lund, Anna Hofmann, Renee Kroon, Ruben Sarabia-Riquelme, Matthew C. Weisenberger and Christian Müller

Submitted Manuscript

CONTRIBUTION REPORT

Paper I	Co-author. Significant contribution towards the electrical characterisation of the foams and all thermal conductivity measurements. Participation in interpretation of the results.
Paper II	Co-author. Responsible for the making of and characterisation of all films and materials electrically and thermally, except those specifically used in the thermoelectric module. The writing of the experimental that I undertook with input towards manuscript and project development.
Paper III	Main author. Responsible for the concept of the work and for the dying characterisation of the yarns. The fabrication and measurement/use of the 'jumbo' thermoelectric module. The writing of the first draft of the manuscript and later iterations, and leading the project.
Paper IV	Main author. Responsible for the concept of the work and for the coating and characterisation of the yarns. The fabrication and measurement/use of both the smaller and the 'mega' thermoelectric module. The writing of the first draft of the manuscript and later iterations, and leading the project.

PUBLICATIONS NOT INCULUDED IN THESIS

Paper V **Thermoelectric plastics: from design to synthesis, processing and structure–property relationships**

Renee Kroon, Desalegn Alemu Mengistie, David Kiefer, Jonna Hynynen, Jason D. Ryan, Liyang Yu and Christian Müller

Chemical Society Reviews, 45 (2016), 6147

Patent I **A process for obtaining an organic n-type semiconductor by irradiating UV-VIS**

Mariano Campoy-Quiles, Alejandro R. Goñi, Bernhard Dörling, Christian Müller and Jason D. Ryan

Spanish Patent, ES2613546B1, (2018)

CONTENTS

Chapter 1

INTRODUCTION

Thermoelectrics, first observed by Thomas J. Seebeck in 1821, is the name given to describe the general process of electrical potential generation from an electrical conductor or semiconductor when put in contact with a heat source, leading to the ability to drive a current. Heat is an abundant but often wasted source of energy, which can be directly converted into electricity using thermoelectric generators that exploit this so-called Seebeck effect. Notably, this effect is not just a one way system, the converse Peltier effect (Jean Peltier, 1834) can be used to convert electrical energy into thermal energy via the application of an electrical current, to the same type of device. This Peltier effect offers particular interest towards both spot cooling and heating applications. Thermoelectric generators are robust devises that exist in the solid-state, containing no moving parts, leading to low maintenance and long life. A significant plus point of such thermoelectric generators is the possibility to utilise small heat sources and temperature differences, which offers particular application where traditional heat engines cannot be used. Unfortunately, high costs of commercially available thermoelectric devices and systems do not allow for widespread use, such as in the average person's home. Currently, high performing inorganic thermoelectric devices exist as metal alloys, such as the well performing bismuth telluride types, however these are expensive to produce on a small scale and contain toxic elements, including lead, antimony and tellurium. This dramatically limits the use of these devices to niche applications such as costly wrist watches which harvest waste body heat, and radioscopic thermoelectric generators which help to power space craft and lighthouses by harvesting heat given off from decaying radioactive materials.

Lying in contrast to the afore mentioned devices, is thermoelectric plastics, i.e. mouldable polymer based materials, which are able to be shaped easily into a wide range of geometries, from simple thin film to complex bulk architectures, and give way to an

interesting alternative by promising more cost-effective processing from the melt or solution. Conjugated polymers, based upon abundant elements – namely carbon, oxygen, sulphur and nitrogen – possess easily tuneable structures, which can be achieved by utilising a vast library of polymer chemistry methodologies. Additionally, these polymers offer advances of mechanical robustness and flexibility, light weight and usually low thermal conductivities. In recent years the knowledge surrounding high throughput coating and printing of large-area electronics (for use in, for example, logic circuits, flexible displays and solar cells) has significantly advanced and can be transferred to the development and fabrication of thermoelectric modules, and for a specific example, the proof of concept study by Søndergaard et al.[1] could be viewed. Textile manufacturing, which has garnered limited attention for organic electronics, lends itself as an alternative given that they are readily compatible with the small, millimetre-thick dimensions of a well-designed thermoelectric generator. The broad range of potential harvesting applications for thermoelectric plastics include large area devices for waste heat recovery on an industrial scale, for temperatures of up to approximately 200 ºC, such as chimney cladding, pipes and high-voltage power cables. Conversely, flexible and small-scale generators could be used to expand the reach and charge lifetime of autonomous electronics as part of the 'internet of things', which in the case of textiles, would be powered by waste body heat.

Chapter 2

THERMOELECTRICS

This thesis will focus on organic materials, with their processing and use described in greater detail over the next chapters. However, it is important to note that several inorganic thermoelectric devices are either in operation today or in advanced development stages. Some can be used at home to harness heat energy from stoves,[2] and some have possible application in industry such as within commercial jet engines.[3,4] Arguably the most famous device is the 'Multi-Mission Radioisotope Thermoelectric Generator' that powers NASAs Mars Rover (attaining a heat gradient from the decay of an isotope within the generator).[5,6] Drawbacks of inorganic materials for thermoelectrics include high cost, low mechanical flexibility and in some cases toxicity. Organic materials allow for these drawbacks to be alleviated (see Chapter 3 for organic thermoelectric materials).

2.1 Thermoelectric Parameters

A number of parameters exist, which can be characterised in a thermoelectric material, in brief: Seebeck coefficient, α; electrical conductivity, σ; and thermal conductivity, κ. The combination of these parameters gives rise to the dimensionless figure of merit, *ZT*, a measure of how well the material performs thermoelectrically (see equation 10). Discussed here are these parameters and how one might go about attaining experimental values for them.

2.1.1 Seebeck Coefficient

The main factor for thermoelectric power generation arises from the Seebeck effect. A thermoelectric material must experience a temperature gradient to generate a voltage, $\Delta T = T_{hot} - T_{cold}$, with a hot end and cold end. Along this gradient, charge carriers will accumulate at the cold end of the material due to diffusion (figure 1), which is in turn balanced by an arising electrical field. This charge accumulation gives rise to a potential

difference, ΔV. Methodologies for the preparation of such materials will be discussed in greater detail in Chapter 3 of this thesis.

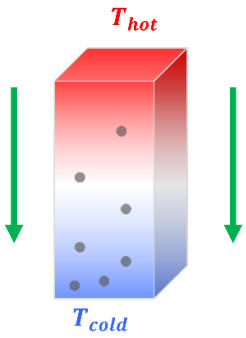

Figure 1. *Schematic of a thermoelectric leg, which experiences a temperature gradient* $\Delta T = T_{hot} - T_{cold}$ *leading to charge accumulation at the cold end. Modified with permission from the Royal Society of Chemistry.*[7]

The temperature-dependent Seebeck coefficient $\alpha(T) = -dV/dT$ can be used to describe a potential difference with units V K^{-1}, and can be understood as the entropy per charge carrier. A high absolute value of α is favourable. For small temperature changes $\alpha(T)$ is almost constant and can be written as:

$$\alpha = -\frac{\Delta V}{\Delta T} \qquad (eq.\ 1)$$

Thermoelectric materials will exist as either p-type or n-type, meaning to say that either holes or electrons, are the majority charge carriers. The sign of α is given from the potential of the cold side with respect to the hot side, thus a p-type material has $\alpha > 0$ and whereas an n-type material has $\alpha < 0$.

A reference type methodology was chosen in order to measure the Seebeck coefficient in all cases presented in this thesis and its respective publications. The device, SB1000, comes from MMR Technologies, USA and with this system the user must only mount a sample on a polyimide sample holder adjacent to a reference sample of typically constantan wire (figure 2). The entire sample holder is then brought up to a selected temperature, here 300 K or 305 K were used to ensure seasonal temperature variations do not affect the sample measurements. Most values for α of organic materials reported in the literature are measured near room temperature. At this point the voltage across the sample and the reference is recorded along with the exact temperature, followed by application of a

current to the resistor in order to heat one end of the sample/reference setup. Then, a further measurement of both the voltages across the sample and reference, and temperature, is made.

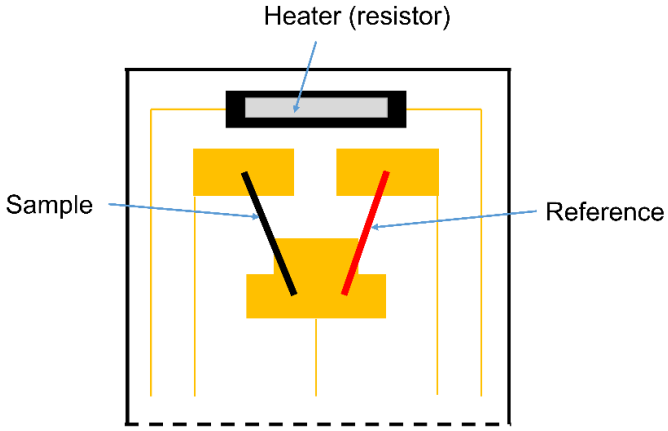

***Figure 2**. Schematic of SB1000 Seebeck sample holder from MMR Technologies, with reference, sample and heater labelled.*

At all temperatures the Seebeck coefficient of constantan, α_r, is known. The voltage difference arising for the constantan reference, ΔV_r, and that for the sample, ΔV_s, are compared in the form of a ratio, which is then used to find the Seebeck value for the sample, α_s, relative to the reference, α_r:

$$\alpha_s = \frac{\alpha_r}{(\Delta V_r / \Delta V_s)} \qquad \text{(eq. 2)}$$

The sample geometry is important in the type of setup chosen, thus the SB1000 was selected because fibres were to be measured. Foams also fit this setup well, in fact, any sample either free standing or mounted on a (non-conducting) support is suitable, as long as the sample is much longer parallel to the temperature gradient direction (≈ 5 mm) than perpendicular (< 1-2 mm). Kemerink *et al*. have discussed that sample geometry, in terms of keeping reference and sample as similar as possible, is important for an enhanced measurement accuracy by limiting the amount of competing conduction paths in the material outside of the region between the electrodes.[8]

Other methods for examining the Seebeck of materials also exist, such as the one used in the ZEM 3L instrument from Ulvac, Germany, relying upon measurements taken only from a sample. Several measurements are made at different ΔT giving different ΔV, with the resulting gradient from a plot of ΔT vs. ΔV being the Seebeck coefficient of the

sample. The SB1000 is advantageous given the quick nature of mounting the samples and reliability of the reference sample, making it more suitable for use of the experiments presented in this thesis.

2.1.2 Electrical Conductivity

The electrical conductivity, σ, is the next essential factor for a thermoelectric material and is intimately linked to the Seebeck coefficient of a sample. The larger σ becomes, the more charge carriers are present in the material, which lowers α as the material is able to achieve less accumulation of charges on the cold side. Further, a power law relationship[9] between α and σ exists as $\alpha \propto \sigma^{-1/4}$. This link between the elements shows that a high electrical conductivity is favourable for both p-type[9] and n-type[10] materials. Electrical conductivity can be described as a product of charge carrier concentration, n, and charge carrier mobility, μ, and the electric charge of a charge carrier, q:

$$\sigma = qn\mu \qquad \textit{(eq. 3)}$$

Much like the Seebeck coefficient, α, a high value of σ is desirable. σ is affected greatly by the nanostructure of the material, where the more ordered the nanostructure is, for example more crystalline, the greater the value for μ tends to be. Further, doping in conjugated polymer systems (transfer of charge carriers) can increase the charge carrier density. An inverse relationship exists between σ and α, especially where doping is involved (See Chapter 3.1.1 for more detail of doping of conjugated polymer systems).

In studies discussed here, numbers for conductivity are often given in the units of S cm^{-1}. However, in reality one measures the resistance, R, of a sample between two points of the material, which is related to resistivity, ρ, an intrinsic property of the sample with length, l and cross-sectional area, A (equation 4). Equation 4 is relevant for measurements made with a 2-point-probe system, which are carried out along the longest dimension of the sample (avoiding competing conducting pathways from interfering, much like the argument made for Seebeck sample geometries by Kemerink *et al.*[8]).

$$\rho = \frac{A \cdot R}{l} \qquad \text{(eq. 4)}$$

ρ, measured in Ω cm, is reciprocated to give conductivity, measured in S cm^{-1}, resulting in the following equation 5, for calculating the conductivity:

$$\sigma = \frac{l}{A \cdot R} \qquad \text{(eq. 5)}$$

In this thesis, several methodologies have been implemented to measure σ. All systems share the fact that current is applied and from the relationship between the applied known current, I, and measured voltage, V, ($R = V/I$) resistance is found. Most often a 2-point-probe system (figure 3a) was utilised using a sourcemeter due to challenging sample geometries in the materials, such as foams and yarns, with the methods available at the time. 2-point-probes contact a sample (usually with a conducting paste at the measuring points to enhance contact with the material) in two places, usually along the direction of interest, and current and measure voltage is applied via the same probes, to give a measure of R and thus σ (figure 3a). However, a disadvantage of this method is that there is also a contact resistance to be accounted for by the probes themselves (and any conducting paste used for electrical contact), which if present, renders the 2-point-probe readings less accurate. The contact resistance in a two-point-probe can be evaluated (as in an experiment conducted with foams in Chapter 4.2) by plotting sample length vs resistance, and if a linear relationship is attained the contact resistance can be corrected for, and if it passes through zero it can be discounted. Contact resistance from the probes can be circumvented altogether in applicable sample geometries, such as in films, with an in line 4-point-probe system, where current is applied through the two outer probes and the two inner probes read the resultant voltage as in figure 3b. Additionally, Bashir *et al*. developed a 4-point-probe system for fibres, thus avoiding contact resistance, which requires a fibre weighted at its ends to rest over 4 cylindrical probes giving a measure of R.[11]

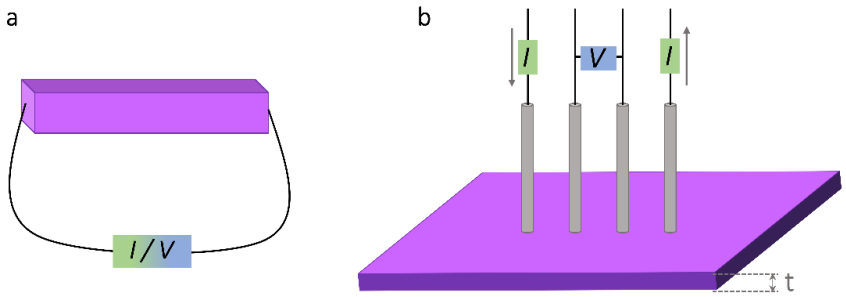

***Figure 3**. Schematics of (a) 2-point-probe measurement to determine resistance, R, of a sample by applying current, I, and measuring voltage, V; (b) 4-point-probe measurement to determine R, avoiding contact resistance by applying I and reading V via different probes.*

The in-line 4-point-probe for films gives a measure of sheet resistance, r_s, with the equation: $r_s = \pi/ln(2) \cdot V/I$, where $\pi/ln(2)$ is a correction factor for when the probes are placed on a film where the distance between the probes is much smaller than the distance between the probes and any boundary of the film (probe to boundary distance > 5*s*, where *s* is the probe spacing). One must then multiply the thickness, *t*, of the sample by r_s to attain ρ and inverse to attain σ:

$$\sigma = \frac{1}{t \cdot r_s} \qquad \text{(eq. 6)}$$

Finally, the van der Pauw method is used for some samples which is similar to the in-line 4-point-probe method, as it still gives us a value for r_s, but the 4 points are no longer in line. The four corners of a square sample film are all contacted and current is applied to two points and voltage measured at the other two, see figure 4a, where the area between points a and b has current applied and points c and d read voltage. This is repeated for all combinations including across the diagonal of the film to give r_s as an average. When performing experiments on thin films (nm range), a correction factor, *F*, is used in lieu of sample thickness, *t*, alone. *F* consists of several factors; a review from Miccoli *et al*. is recommended for more details on *F*.[12] An advantage of this method is the possibility to optimise the sample geometry to alleviate interference from competing conducting pathways. For example, a clover-like sample cutting can be made as shown in figure 4b.[13]

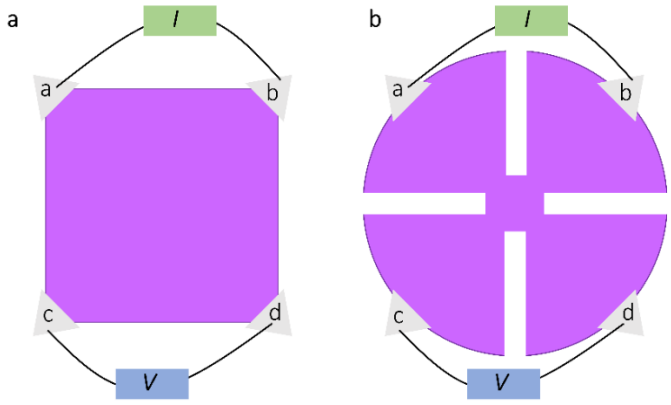

***Figure 4**. Schematic of a Van der Pauw 4-point-probe setup to measure sheet resistance r_s, by applying current, I, and measuring voltage, V.*

It should be noted here, that systems such as the ZEM 3L for Seebeck characterisation can measure α and σ simultaneously via a 4-point-probe method, where the thermal couples are used as the voltage reading probes.

2.1.3 Thermal Conductivity

The last thermoelectric measurement is thermal conductivity, κ, the ability for a material to conduct heat. Most desirable is a low thermal conductivity to avoid thermal losses. This measurement is often the most neglected when reporting the thermoelectric properties of a material. This neglect can arise from problems with sample geometry, for example with fibres, or from a lack of the often expensive materials dealt with, since some measurement techniques require an appreciable amount of material. For systems where a small amount of material is present, techniques that utilise thin films could be recommended (such as the 3-omega method) but for measurement of bulk material, a setup such as the TPS2500, from Hotdisk, Sweden, would be recommended. Measurement of material in the bulk (dimensions of 100s μm and above) is essential, since bulk material will be used in thermoelectric applications. κ exists as a sum of the contributions from phonons and electrons:

$$\kappa = \kappa_{phonon} + \kappa_{elecronic} \qquad \text{(eq. 7)}$$

When we consider the Wiedemann-Franz law (equation 7) we can see the contributions towards $\kappa_{electronic}$ as the product of temperature, T, conductivity, σ, and the Lorenz number, L:

$$\kappa_{electronic} = L\sigma T \qquad \text{(eq. 8)}$$

In equation 7 the Lorenz number, L, is a close-to-constant value of $2.44 \cdot 10^{-8}$ W Ω K^{-2} and has found validity for PEDOT:PSS according to the work of Cahill *et al.*[14] Given this relationship between electron and phonon contributions, materials with low conductivities, such as 1 S cm^{-1}, will essentially possess $\kappa \approx \kappa_{phonon}$ due to a negligible contribution from $\kappa_{electronic} < 0.001$ W m^{-1} K^{-1}. However, when a material starts to possess conductivities in the range of, for example, 100 S cm^{-1}, the electronic contribution towards the thermal conductivity must be considered since it will start to be in the range of κ_{phonon} for the samples (≈ 0.1 W m^{-1} K^{-1}).

The thermal conductivity κ is measured as the product of thermal diffusivity, D, specific heat capacity, C_p, and density, ρ_d:

$$\kappa = D\rho_d C_p \qquad \textit{(eq. 9)}$$

In this thesis, all values of κ have been determined with a TPS2500 setup from HotDisk, Sweden, an offshoot company of Chalmers University of Technology, which utilises the transient plane source technique (TPS). The device works by giving the user experimentally determined values for D and in some cases C_p, with the user inputting ρ_d. In the case of C_p being determined by the sensor in a κ experiment, the sample is believed to be isotropic (equally thermally conducing both radially and axially). A setup also exists for the determination of C_p alone for anisotropic materials (differing thermal conductivities radially and axially), where the sample is placed into a gold cell, heat is applied and the absorbance of that heat compared to a blank (air) sample gives C_p. This value is then used when performing a κ measurement. One may of course also determine C_p with a differential scanning calorimeter (DSC), however all necessary measurements of C_p for this thesis were made with the HotDisk setup.

More specifically, the setup works by the use of a probe sensor placed between two samples of identical material, this usually is a thick bulk material. First, direct current heats

up the sensor, then the heat dissipates into the sensor and sample, the change in sensor electrical resistance is then recorded and converted to sensor temperature increase vs. time, giving us the 'transient curve', which contains information about thermal properties.[15,16] Figure 5a shows an example of a transient curve, in this case from a foamed sample of poly(3-hexylthiophene) from Paper I.

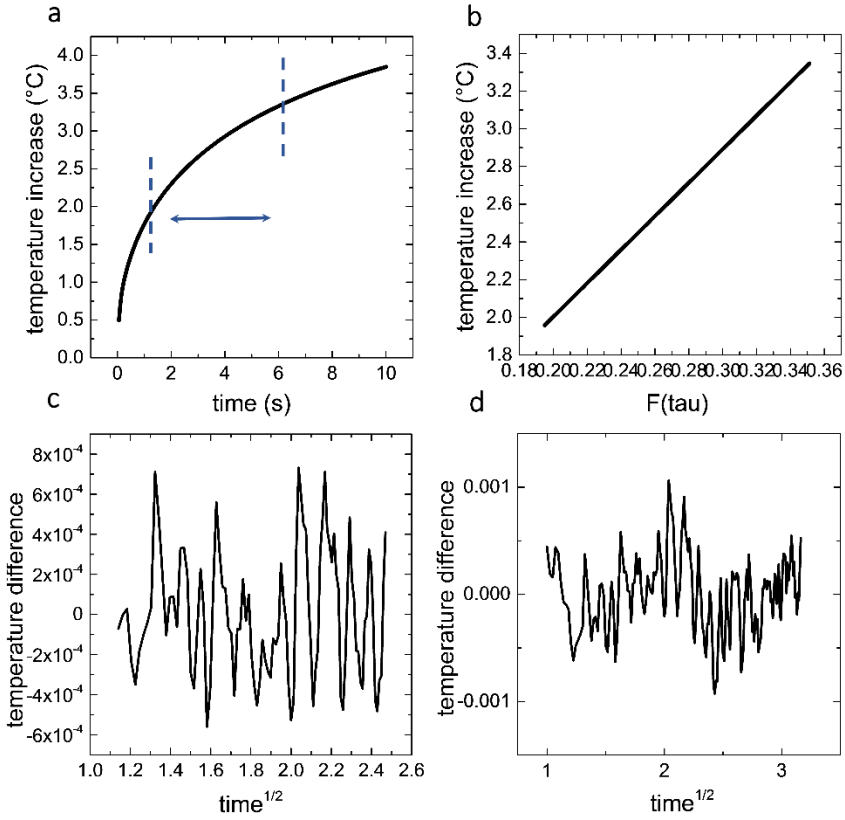

Figure 5. *Example data plots provided by the TPS250 software whilst determining thermal conductivity. (a) Temperature increase of sensor vs. time, containing information about thermal properties; (b) temperature increase of sensor vs. F(tau) (dimensionless time) is plotted from figure 5a blue region; (c) a plot temperature difference vs. time$^{1/2}$ showing a satisfactory selection from figure 5a data blue region and (d) all data selected from figure 5a showing a correlation in data.*

Once the experimental transient curve has been attained, a region of the data is selected for evaluation, for example between the dashed lines in figure 5a, and plotted as temperature increase vs. F(tau) (dimensionless time) (figure 5b). An iteration process is used to select regions of data until a linear relationship is attained when plotting temperature increase vs. F(tau). For further confidence in the linearity in figure 5b temperature difference

vs. time$^{1/2}$ is plotted, which should display no correlation in the data (figure 5c).[17] For more details on the TPS technique see a work by Krupa *et al*. who demonstrate its use on aluminium-silicate materials.[15]

Measurements can also be made with films (20 to 1000 µm thick) which relies on having a highly thermally conducting, usually metallic, sink as a blank reference. Figure 6 shows a schematic of the sensor on a thick material (one sample piece shown for clarity), with the heat dissipating into the sample from the sensor (dark red to light red).

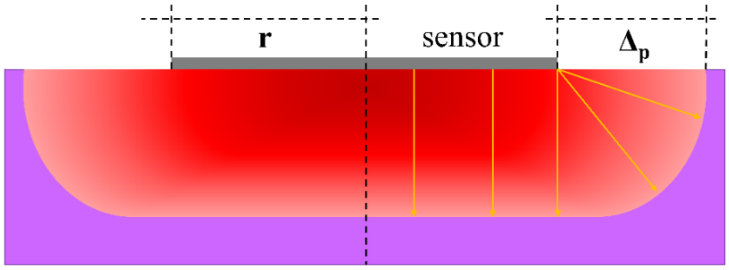

***Figure 6**. A TPS250 sensor from Hotdisk on a bulk sample (one sample piece is shown for clarity), with heat dissipating into the sample from the sensor (yellow arrows). r = sensor radius, Δ_p = probing distance.*

Some considerations should be made for probe size selection, such as the radius of the sample relative to the probe, $r \leq \Delta_p \leq 2r$, and that the heat should ideally not reach any sample boundaries; however if the heat does reach the sample boundary, this region can be disregarded in the iteration process of region selection for analysis. If the heat were to reach a boundary, it would be visible in the plot of temperature difference vs time$^{1/2}$ when all data is selected (not just one region), for example, by a sharp change in trend of the data points as time$^{1/2}$ progresses (figure 5d). Further, the optimal experimental measurement time, *t*, can be estimated with $t = \Delta_p^2/4D$, where *D* is estimated initially so then *t* can be fine-tuned after the initial experiment.

Another possibility for determining κ would be to use a 3-Omega setup, which was originally developed by Corbino *et al*. to measure the thermal diffusivity of metal filaments used in incandescent light bulbs.[18] This setup requires a thin film (thickness < 1 µm) upon a substrate to have a heater line deposited upon via photolithography or shadow mask evaporation. Usually this method is used to measure axial thermal conductivity only. This

method was decided to not be suitable for use in this thesis' projects due to the geometry of the samples required.

2.1.4 Figure of Merit

To give a measure for how good a thermoelectric material performs, as a combination of the three above discussed factors of Seebeck coefficient, α, conductivity, σ and thermal conductivity, κ, we can use the dimensionless thermoelectric figure of merit, ZT:

$$ZT = \frac{\alpha^2 \sigma}{\kappa} T \qquad \text{(eq. 10)}$$

The larger the value of ZT, the better the thermoelectric material can convert heat into electricity. α and σ have an inverse relationship; doping levels can be varied to adjust α and σ, as an increase in charge carriers increases σ but decreases α.

A current 'gold standard' inorganic material is bismuth telluride with a ZT ≈ 1 at room temperature, with some organic materials reaching values of ZT ≈ 0.2.[19] Some materials will unfortunately possess challenging geometries for the determination of κ, so instead the power factor of a material, $\alpha^2\sigma$, is often reported, giving a value that can still be used to compare differing materials in terms of their electrical properties.

2.2 Thermoelectric Generators

So far the parameters for the characterisation of a thermoelectric material have been discussed along with their merit. The next step in the 'journey' of these materials is their use in a thermoelectric generator. The most fundamental unit of a thermoelectric generator is the thermocouple, which is comprised of a 'leg' of p-type material and a 'leg' of n-type material connected together electrically in series and thermally in parallel, as shown in figure 7.

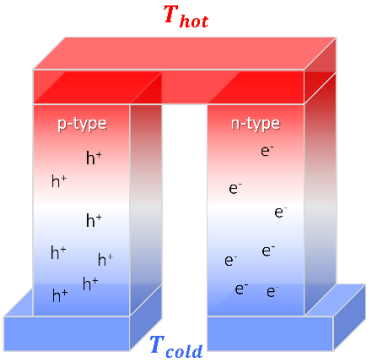

***Figure 7**. Schematic of a thermoelectric element, which comprises one n- and one p-type thermoelectric leg that experience a temperature gradient, ΔT, leading to charge accumulation at the cold ends. Reproduced with permission from the Royal Society of Chemistry..*[7]

Suitable organic n-type materials are rare and instead a p-type material can be used as a substitute[20-23] (see Chapter 6.3), as long as the substitute Seebeck coefficient is as close to zero as possible to ensure that the opposing Seebeck values of the p-leg and 'n-leg' do not cancel out (see Chapter 2.2.1, equation 11).

2.2.1 Open Circuit Voltage and Power

A single thermocouple produces a too low thermovoltage, in the range of a few millivolts, at expected organic material operational temperatures, which is too small to power electronic components (at least one volt is needed). In order to bypass this issue, we can create devices with many thermocouples, connected electrically in series and thermally in parallel (figure 8).

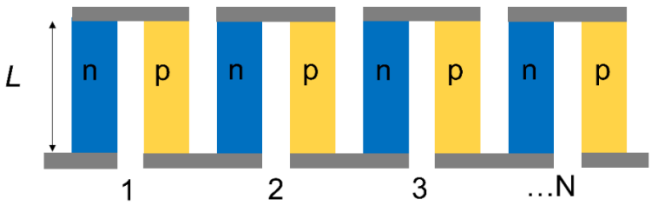

***Figure 8**. Schematic of a row of N elements, thermally connected in parallel and electrically connected in series.*

As touched upon previously, the values of α for the two legs must be composed of different materials with different Seebeck coefficients, $\alpha_{\text{p-leg}}$ and $\alpha_{\text{n-leg}}$. From this it is clear

that the most efficient design of a thermocouple would be to have p- and n-type materials, rather than a low α p-type material as a substitute n-type leg (equation 11, $N_{element}$ is the number of thermocouples). This gives an open circuit voltage, V_{oc}, according to:

$$V_{oc} = N_{element}(\alpha_{p-leg} - \alpha_{n-leg})\Delta T \qquad \text{(eq. 11)}$$

Electric power, P, is measured in watts and represents the rate in which electrical energy is transferred by an electric circuit. Maximum power, P_{max}, is the most power a thermoelectric device can provide and is only obtained upon load matching when the internal resistance, R_{int}, and the applied external load, R_{load}, of the generator are equal, i.e. $R_{int} = R_{load}$, and can be related to V_{oc}:

$$P_{max} = {V_{oc}}^2/4R_{int} \qquad \text{(eq. 12)}$$

It is noted that V_{oc} is dependent on $N_{element}$, whereas P_{max} is strictly 'per area' and independent on $N_{element}$ since R_{int} increases accordingly with more legs added. Assuming that R_{int} is kept constant, P_{max} is found by varying R_{load} until a maximum is found (figure 9).

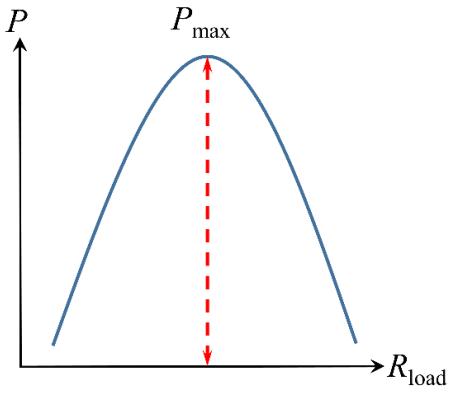

***Figure 9**. An example sketch of power vs. load resistance, R_{load}; where R_{load} is varied to until $R_{load} = R_{int}$ to attain P_{max} for a set V_{oc}.*

Given the necessity for $R_{int} = R_{load}$ to attain a maximum power, each thermoelectric generator must be tailored in terms of R_{int} for a specific purpose to coincide with the R_{load} related to the task performed. R_{int} can be tuned by the design of the thermoelectric generator, specifically the cross-sectional areas, A, of the legs to adjust the cumulative value of R, which gives R_{int}, from both legs.

To acquire a larger P_{max}, R_{int} should be as small as possible. For a module with a set thermoelectric element cross-sectional area, where $A_n + A_p$ is constant, the ratio between the legs' area should be considered in order to attain a minimal R_{int}. The resistances can be related to the electrical conductivity, σ, of the leg's material (equation 13). A_p and A_n, represent the areas of p- and n-type legs' respectively, as with σ_a and σ_n representing the electrical conductivity of the legs respectively:

$$\frac{A_n}{A_p} = \sqrt{\frac{\sigma_p}{\sigma_n}} \qquad \text{(eq. 13)}$$

Upon optimisation of the legs' area, whether in minimising R_{int} without regard to area or optimising the p-/n-legs area ratio for a set total area, the P_{max} of the system will be improved to its maximum potential, given the materials used.

2.2.2 Generator Design

Two main design types can be considered to apply to most, if not all, cases of thermoelectric generators, in-plane and out-of-plane, figure 10a and 10b respectively. An out-of-plane device maximises the useable space by allowing for a greater amount of legs per area by harnessing temperature differences on end or vertically as in figure 10b, rather than requiring an in-plane heat source as with figure 10a.

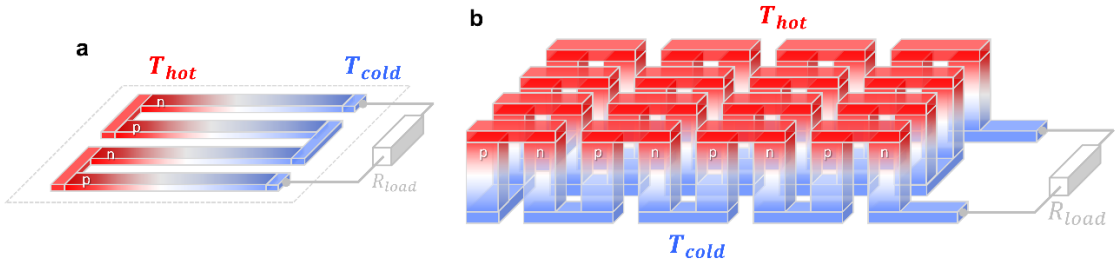

***Figure 10**. Schematics of (a) an in-plane (printable) array of elements and (b) a conventional thermoelectric module that comprises an array of elements, which are connected electrically in series but thermally in parallel. A load resistance R_{load} is connected to close the circuit, resulting in maximum power generation when $R_{load} = R_{int}$. Reproduced and modified with permission from the Royal Society of Chemistry.*[7]

This thesis predominantly explores the developed thermoelectric materials with in-plane devices, specifically, in Papers III and IV. In particular, in-plane modules have been used to evaluate the processing and development of the materials, without focus on optimisation of the generators themselves. The reader is directed to a detailed review by He *et al*. for a summary of recent thermoelectric generator architecture developments.[24] Future work following this thesis should focus upon out-of-plane modules, given that materials have now been developed (see Chapter 7).

Sun *et al*. have demonstrated an origami, or corrugated, approach to developing an out-of-plane thermoelectric module.[25] Firstly, the thermoelectric material is printed as a film (figure 11a), then the material is folded by heat shrinking to form a 3D out-of-plane device (figure 11b). The folding of a film is very useful, and lends itself well to industrial upscaling with reel-to-reel processing. Further module designs include such architectures as a ring structured cylinder[26] and coin-sized coil,[27] which are also used in an out-of-plane manner.

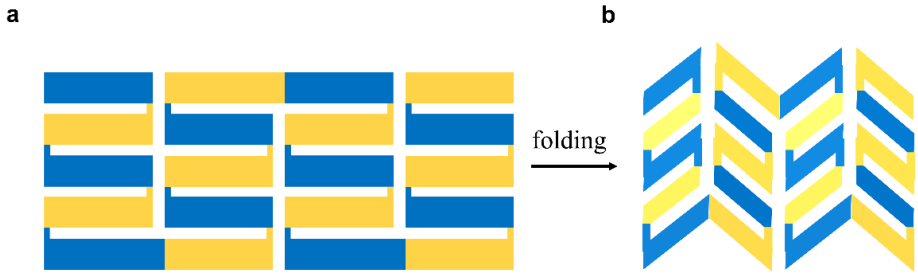

Figure 11. *Schematic of an origami thermoelectric module being folded, from (a) to (b).*

Fabián-Mijangos et al. discuss a further modification to a more conventional out-of-plane bulk device (figure 10b) by shaping the legs in a pyramid fashion.[28] This design has the legs thicker at one end and thinner at the top, which allows for ≈ 70% enhancement in power output in a reported inorganic device.[28] This design may find applicability in organic systems which utilise bulky architectures, such as foams.

Chapter 3

ORGANIC THERMOELECTRICS

Organic materials such as conjugated polymers and carbon nanotubes are currently of great interest in the field of organic thermoelectrics. When compared to inorganic thermoelectric materials, organic semiconductors are more favourable in regard to cost, toxicity, processability and importantly, air-stability. Further, organic based materials are advantageous (c.f. inorganic) due to their versatile portfolio of mechanical properties such as elasticity, ductility and high tenacity. Hence, organic materials lend themselves particularly as textile coatings or materials for fibre production[29] (see Chapter 6 for expansion on textiles). Some organic state-of-the-art materials, possessing high power factors are noted: the p-type system of PEDOT:PSS with DMSO and PEG, possessing a *PF* of 157 μW m^{-1} K^{-2};[30] the polythiophene PBTTT vapour doped with F4TCNQ, *PF* = 120 μW m^{-1} K^{-2};[31] n-type materials have also had breakthroughs with *PF*s as high as 236 μW m^{-1} K^{-2} using the small molecule A-DCV-DPPTT and dopant nDMBI.[19] See appendix of this thesis for a detailed list of all mentioned polymers, their structures and abbreviations.

Much attention is currently given to the study of organic materials in the form of thin films (thicknesses in the 10s – 100s nm). Studying thin films is a good way to attain fundamental knowledge of a system, such as information regarding its nanostructure. However, moving forward to use these materials in a practical, functional way, their study must be focused towards bulk architectures, since this is ultimately how organic materials are likely to be used (thicknesses of 100s μm to several mm).[32] Further, most, if not all studies on thin films account only for the conducting material in question, and do not include the substrate in the thermoelectric parameters (such as those in Chapter 2). Self-folding thin films as a method towards attaining thick millimetre structures is a route explored in several works, where stimuli such as light,[33] stress,[34,35] heat[36] and pH[36] are used. In this thesis, work has been undertaken to use thermoelectric systems realistically in the bulk, such as in foams and textiles where the whole material including air (in the case of foams) and insulating cores and coatings (in the case of textiles) is accounted for, allowing for an accurate calculation of thermoelectric parameters.

In the following sections of this chapter 3, organic materials will be discussed more specifically, but in brief it is useful to introduce the "tetrahedron of thermoelectric plastics" (figure 12),[7] which illustrates essential building blocks to be utilised towards effective thermoelectric plastic design. This thesis touches upon each building block in different combinations with one another, such as the doping of conjugated polymers (Paper I), conductive fillers with conjugated polymers (Paper II), conjugated polymers with counterions (Paper III) and conductive fillers with polymeric dopants (Paper IV). The use of insulating polymer support structures, in the form of yarns (Papers III + IV), is also featured.

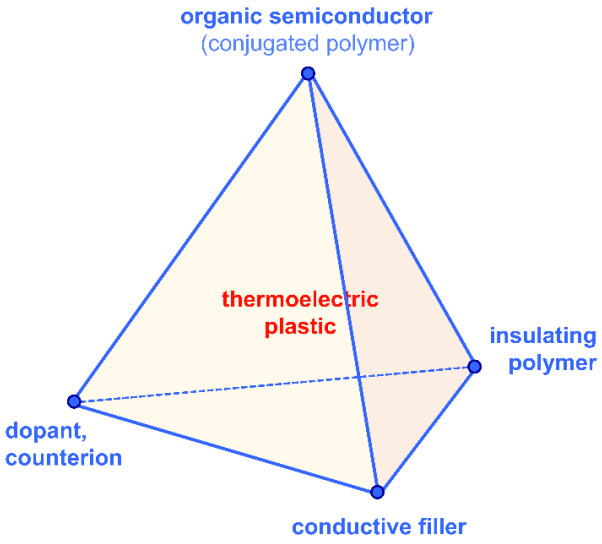

***Figure 12**. The tetrahedron of thermoelectric plastics, illustrating the four main building blocks: (1) organic semiconductors and in particular conjugated polymers, (2) dopants and counterions, (3) insulating polymers, and (4) conductive fillers such as carbon nanotubes, graphene and inorganic semiconductor nanowires. Reproduced with permission from the Royal Society of Chemistry.*[7]

3.1 Conjugated Polymers

A significant breakthrough in the use of conjugated polymers came when Alan J. Heeger, Alan MacDiarmid and Hideki Shirakawa reported on their work with polyacetylene and its notable increase in conductivity upon doping with iodine.[37] Since this discovery, it is certainly correct to state that research on conjugated polymers has significantly increased.[38]

Conjugated polymers are polymeric species, which consist of an alternating single-double bond backbone with a delocalised electron system. There are many ways to design and synthesise a multitude of different conjugated polymers, in fact a toolbox of methods can be utilised, some of which are summarised in the reviews of Kroon *et al.*,[7,39] Liu *et al.*[40] and Gedefaw et al.,[41] which the reader is referred to for further reading.

Figure 13 shows the build-up of a double bond between two carbon atoms. Each carbon possesses four valence electrons and in this case one electron from each carbon is dedicated to the σ-bond that is formed between the hybridised sp^2 orbitals, and one electron from each carbon is dedicated to the formed π-bond across the p-orbitals, to form a double bond overall. Of course, a further electron in each of the other two sp^2 orbitals forms a single bond to another atomic species. The π-electron in a conjugated system is free to undergo interactions with external stimuli such as light and redox species while the σ-bond ensures structural integrity.

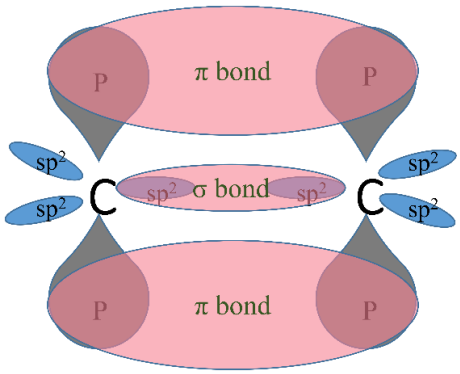

***Figure 13**. Schematic of the molecular orbitals of a double bond between two carbon atoms.*

A splitting of energy levels will occur with increased conjugation (figure 14), this leads to what is known as a valence band and a conduction band, with the highest occupied molecular orbital (HOMO) and lowest unoccupied molecular orbital (LUMO) bordering each band, respectively, as shown in figure 14. The energy gap between the HOMO and LUMO is defined as the band gap, the energy necessary to excite an electron from the HOMO to the LUMO, which typically exists between 1.5 – 3 eV. As energy level splitting continues with higher degrees of conjugation, the HOMO and LUMO begin to converge and the bandgap becomes progressively smaller.

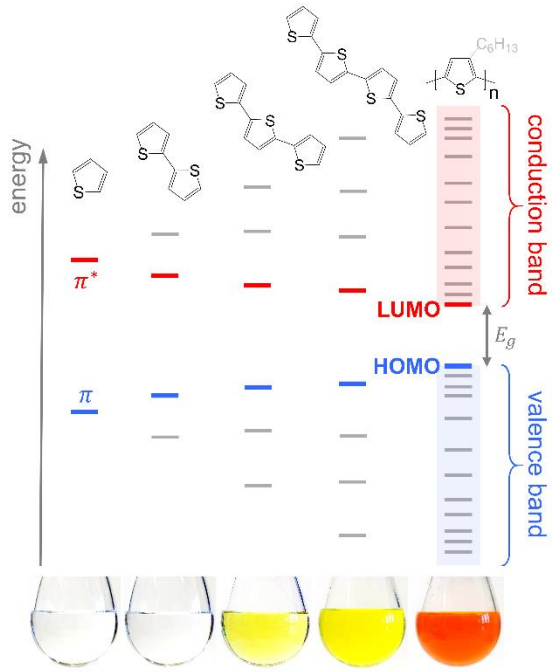

***Figure 14**. Evolution of the HOMO and LUMO levels as well as bandgap E_g with increasing number of thiophene repeat units, resulting in valence and conduction bands for polythiophene; the images of 5 g L^{-1} solutions in chloroform illustrate the narrowing of E_g, which leads to a red-shift in absorption (the polymer is P3HT). Reproduced with permission from the Royal Society of Chemistry.*[7]

3.1.1 Doping Conjugated Polymers

Conjugated polymers themselves would not be of great interest electrically in thermoelectrics if not for the possibility to dope them to increase their charge carrier concentration. Doping is the term given to the transfer of charge carriers from one species to another, where the 'dopant' is defined as the "Charge-transfer agent used to generate, by *oxidation* or *reduction*, positive or negative charges in an intrinsically conducting polymer".[42] Through doping, free charge carriers are introduced to a conjugated polymers backbone and conductivity, σ, is increased, however in most cases causes a decrease of its Seebeck coefficient, α.

There are a few different routes towards doping of conjugated polymers, with figure 15 showing schematically both acid-base doping[31,43] and redox doping.[44,45] Acid-base doping is the transfer of a H^- (for n-type doping) or H^+ (for p-type doping) to the backbone

of the polymer, where a counter ion derived from the hydride/proton source will be present in order to maintain overall neutrality of the species. Redox doping is the transfer of an electron between the conjugated polymer and a donor/acceptor molecule, leading to the formation of an ion pair. Figure 15 shows schematically how the HOMO level of the donating species must be higher than the LUMO of the receiving species.

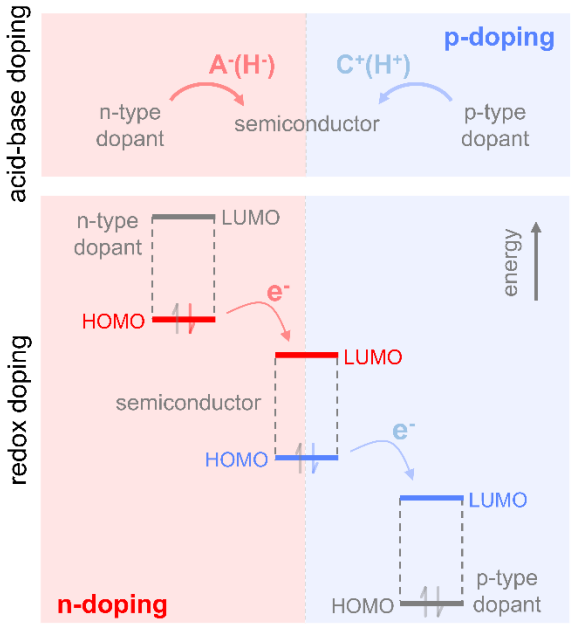

***Figure 15**. (Top) the basic principle of acid–base doping, which involves the transfer of an anion (H^-) or cation (H^+) to the semiconductor; and (bottom) redox doping, which involves the transfer of an electron to the LUMO or from the HOMO of the semiconductor in the case of n- and p-doping, respectively. Reproduced with permission from the Royal Society of Chemistry.*[7]

Another example of dopant type is small Lewis dopants, such as I_2,[46] $FeCl_3$[47] and tris(pentafluorophenyl)borane (BCF).[48] BCF has found use in doping high ionisation energy polymers such as IP-TT, an indenopyrazine polymer, which another common molecular dopant 2,3,5,6-Tetrafluoro-7,7,8,8-tetra-cyanoquinodimethane (F4TCNQ) was unable to dope.[49] Each doping method undertaken leads to the formation of a polaron (a radical anion or cation). These charges are delocalised over several monomer units of the polymer and in some cases a high doping level can lead to the combination of two polarons forming a bipolaron (figure 16).

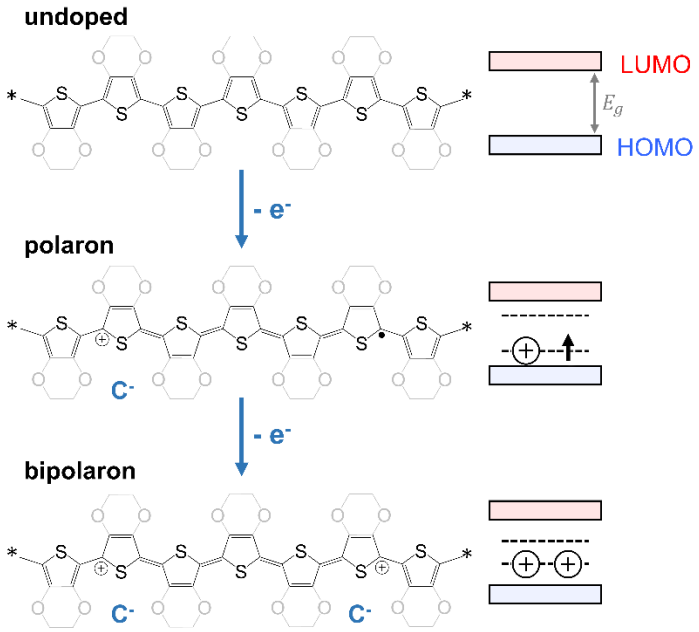

***Figure 16**. Schematic for p-doping of polythiophene and PEDOT (left) and the corresponding band structure evolution (right): electron transfer (-e⁻) to the undoped polymer (top) leads to the formation of a polaron (middle) and finally a bipolaron state (bottom); counterions (C⁻) ensure charge neutrality. Reproduced with permission from the Royal Society of Chemistry.*[7]

3.1.2 Specific Doping Examples

Two conjugated polymers of major focus in this thesis are poly(3-hexylthiophene) (P3HT) and poly(3,4-ethylenedioxythiophene) (PEDOT) (see appendix). Both polymers are based upon functionalised thiophene monomer units.

P3HT:F4TCNQ

In their unsubstituted form, conjugated polymers, such as polythiophenes, are intractable. A common way to increase their processability is to functionalise them with alkyl side chains in order to attain solubility in organic solvents. P3HT is a perfect example, where the addition of an alkyl chain to an unsubstituted polythiophene, gives the functionalised poly(3-alkylthiophene). P3HT is available in a large range of molecular weights (Mn 20-50 kg mol^{-1}) and regioregularities, which dictates its solubility and processability. Charge carrier mobility increases with increasing regioregularity of P3HT[50,51] and also with increasing molecular weight of P3HT (saturating at 25 kg mol^{-1}).

P3HT and the molecular dopant F4TCNQ (see appendix) is a highly studied redox doping system.[51-55] Figure 17 (left) shows a schematic representation of the doping between P3HT and F4TCNQ. Importantly, the HOMO level of the donor (P3HT) is higher than that of the acceptor (F4TCNQ) leading to p-doping of the P3HT via transfer of an electron to F4TCNQ. Figure 17 (right) shows another common dopant DDQ with a LUMO level too high in energy for P3HT to donate an electron and to become p-doped.

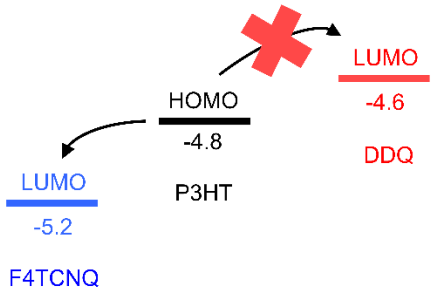

***Figure 17**. Schematic of p-doping P3HT with F4TCNQ and unsuccessful doping with DDQ.*

PEDOT:PSS

PEDOT is an interesting case of a conjugated polymer that is synthesised in its conducting form. In fact, PEDOT, which on its own would be intractable, is polymerised using polystyrene sulfonate (PSS) as a scaffold, which then ultimately acts as a counter ion. Two main methodologies exist to synthesise PEDOT:PSS, namely oxidative polymerisation and electrochemical polymerisation, both produce a conducting p-doped PEDOT material. Electrochemical polymerisation allows other counterions to be introduced such as tosylate, sourced from $Fe(Tos)_3$, to form PEDOT:Tos.[56] Another difference with PEDOT:PSS (figure 18) compared to other common polymers is the significantly lower molecular weight of the PEDOT, consisting of approximately 6-18 monomers.[57]

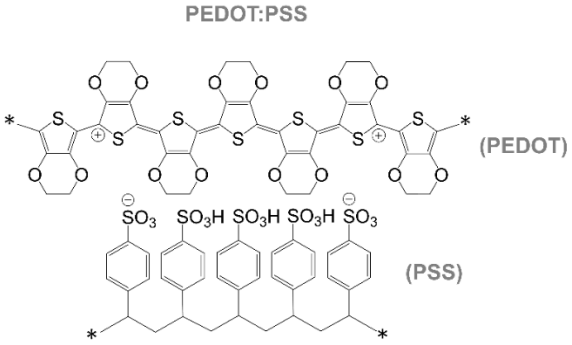

***Figure 18**. Chemical structure of PEDOT:PSS; with the PEDOT carrying a bipolaron.*

PEDOT by itself is not water processable, but given that PSS is water soluble, the overall PEDOT:PSS complex can processed in aqueous media – the PSS will surround the PEDOT in a core-shell type conformation where the sulfonate ions stabilize the nanoparticle suspension against coagulation (figure 19).

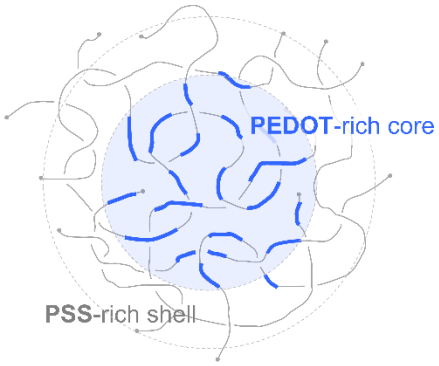

***Figure 19**. Core-shell structure of a PEDOT:PSS complex in an aqueous dispersion. Reproduced with permission from the Royal Society of Chemistry.*[7]

The conductivity of PEDOT:PSS ($\sigma \approx 10$ S cm^{-1}) can be improved by the addition of 'secondary dopants' in solution such as dimethylsulfoxide (DMSO), ethylene glycol (EG) or exposure to methanol once dried ($\sigma \approx 10^3$ S cm^{-1}). These secondary dopants do not actually add charge carriers to the system, but affect the nanostructure (and charge carrier mobility) and such changes remain when secondary dopants are removed.[57]

3.2 Carbon Nanotubes

Referring back to the tetrahedron of thermoelectric plastics (figure 12), a key building block is the use of conductive fillers. Nanocomposites, the combination of conductive fillers and polymers are a widely used approach[38,58] to improve thermoelectric properties.

Carbon nanotubes (CNTs) are conductive fillers that have received great attention for their high mechanical strength, and high electrical and thermal conductivities (intrinsically: $\sigma = 10^4$ S cm^{-1} and $\kappa = 10^3$ W m^{-1} K^{-1}). Two main forms of CNT exist, namely, single-walled (SWNTs), made of a single sheet of graphene rolled up into a cylinder with typical diameters of 1.2 – 1.4 nm; and multi-walled (MWNTs), consisting of several single tubes nested inside each other. MWNTs are the main focus of this thesis, which tend towards

being metallic in behaviour (SWNTs can be either metallic or semiconducting in behaviour and are challenging to separate after synthesis).

CNTs can be up to several micrometers in length and tend to aggregate into bundles, leading to the necessary use of surfactants and shear (through sonication if solution processed) in order to disperse them in a solvent or a polymer matrix. However, once the CNTs have been exfoliated a relationship between conductivity and concentration can be observed. Figure 20a shows a generic graph where the concentration, *c*, of CNTs in a less conducting matrix is plotted vs σ and α. Once the percolation concentration of the CNTs (the formation of a connected network throughout the material) is reached, *c**, the (in this case) much greater conductivity of the CNTs begins to dominate and σ becomes larger towards that of the pure CNTs. Since the Seebeck coefficient in a nanocomposite is given by the more conducting phase, at and above *c** the value of α is also given by the Seebeck of CNTs. Figure 20b schematically shows CNTs in a polymer matrix below ($c < c^*$), at (c^*), and above percolation ($c > c^*$), where the CNTs form a connected conducting network through the matrix.

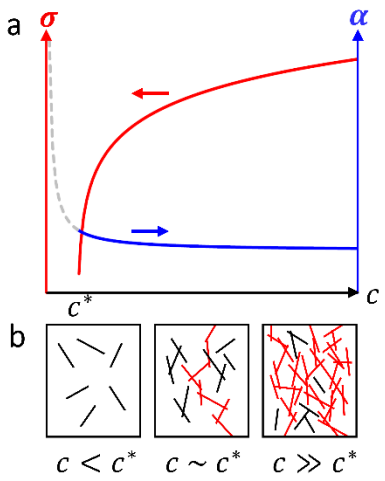

Figure 20. *Evolution (a) of the electrical conductivity σ and Seebeck coefficient α with concentration c of an anisotropic conductive filler in a less conductive polymer matrix; filler particles (b) form continuous conducting pathways (red) above the percolation threshold c*. Reproduced with permission from the Royal Society of Chemistry.*[7]

CNTs are of great interest in thermoelectrics given their high electrical conductivity along with the fact that a rather low filler content is actually required before percolation occurs. This low threshold is ascribed to the high aspect ratio of the CNTs.

3.2.1 Doping Carbon Nanotubes

CNTs tend to exhibit unipolar p-type behaviour in air due to oxygen doping, but are ambipolar in vacuum. Unipolar materials are those with a charge carrier majority of either holes or electrons, whereas ambipolar materials possess no charge carrier majority but have the potential to accumulate either.[59] Treating CNTs with either oxidising or reducing agents allows for the tuning of the CNTs p- or n-type behaviour, respectively. Nonoguchi *et al*. present a detailed report on a panel of p- and n-type dopants for use with CNTs.[60]

A popular way to change the behaviour of CNTs towards n-type behaviour is to actually incorporate nitrogen atom defects into the CNT during synthesis.[61] These carbon nanotubes will have an inherent air stable n-type behaviour and have shown the ability to engage in charge transfer with P3HT, a process more pronounced in iron containing samples, and proven with photoluminescence quenching[62] (see Chapter 5 for more detail).

This thesis also explores in greater detail the doping, or rather, charge induction to MWNTs using the polymeric dopant polyvinylpyrrolidone (PVP) as observed by Sarabia *et al*.[63] Chapter 6 discusses how PVP can alter MWNTs from p- to n-type for use in conducting yarns for thermoelectric textiles.

Chapter 4

FOAMS

The foaming of plastics is an advantageous method for tuning the physicochemical properties of a material, utilising pore size, connectivity of the pores and porosity.[64] Plastic foams have found use in many day-to-day industries, in particular, due to a high possible degree of compression, they are commonly found in food packaging and cushioning. Further, given their low thermal conductivity, due to the inclusion of air in the foam, they are used for refrigerated food delivery, insulation in building construction[65,66] and diving wetsuits. It is possible for the foam's pores to be impregnated by gasses and liquids, for example, by air and the doping solution as in the appended Paper I, and water, as in collagen sponges.[67]

This chapter will focus on poly(3-hexylthiophene) (P3HT) foams with porous air pockets. In particular, the inclusion of the p-type dopant 2,3,5,6-Tetrafluoro-7,7,8,8-tetra-cyanoquinodimethane (F4TCNQ) and its effect on the foam's conductivity, σ, and Seebeck coefficient, α. Additionally, the effect of pores on the thermal conductivity of the foam compared to bulk P3HT without pores and the overall figure of merit, *ZT*, of the material.

Doping of thick bulk material (millimetre scale and above), c.f. thinner samples (micrometre scale and below), is notoriously difficult, since the most effective methodology leading to superior thermoelectric materials, is to sequentially dope a conjugated polymer system.[37,55,68,69] Sequential doping is the inclusion of a dopant into a solid material such as films (figure 21). However, sequential doping is diffusion limited, and in a bulky millimetre thick system not a feasible method to utilise since the dopant cannot penetrate the whole material in a reasonable time or, in some cases, at all. As a result of limited diffusion, a part of the material is essentially rendered as useless and will only negatively contribute to the thermoelectric properties of the material such as electrical conductivity. The converse approach to sequential doping would be to include the dopant within the polymer matrix whilst in solution and form the solid material together with the dopant, a method known as coprocessing (figure 21). While this form of coprocessing of the dopant and polymer together is a practical way of getting a dopant to all parts of the subject material,[9,70] it is ruled

out as being the most effective path given that sequential doping allows for optimisation of the nanostructure of the semiconductor before doping.[32]

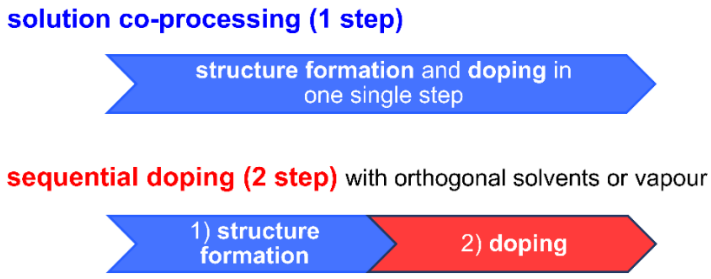

Figure 21. *Flow diagram comparing doping through coprocessing (top) and sequential doping (bottom).*

Dopant molecules are assumed to diffuse through a solid polymer matrix when heated above the glass transition temperature, T_g, of the polymer. A study by Moulé *et al.*[71] demonstrated that F4TCNQ diffuses at room temperature since P3HT will be above its T_g of 12 ºC.[72] Dopant diffusion through a solid matrix can be complicated, with both neutral and charged dopant complexes existing. For example, neutral F4TCNQ possesses a diffusion coefficient (a measure of diffusion as a function of distance and time) in the order of $\approx 10^{-14}$ cm^2/s, whereas the charged species has a diffusion coefficient 2-3 orders of magnitude slower.[55,73] An advantage of foamed polymers is that the dopant can be delivered directly to all parts of the material via interconnected pores, then diffuse into the polymer from inside the structure.

4.1 Foam Manufacture

There are several ways to manufacture foams, including lyophilisation,[74] foaming gas agents[75] and utilising thermally induced phase separation (TIPS).[76,77] Lyophilisation is the removal of solvent from a frozen solution under vacuum, leaving behind a foam of the polymeric material, which has been used in some cases with PEDOT:PSS.[78] In paper I, we discuss the use of TIPS to manufacture a polymer foam of P3HT. The methodology was adapted from the work of Heijkants *et al*. who fabricated polymeric foam scaffolds for use in the medical devices field. In the work of paper I, the manufacture of the foam was developed by Dr Renee Kroon, of Chalmers University, by using salt (NaCl) to introduce micrometre-sized pores, the size of which can be controlled by the size of the salt crystals

used. TIPS was used to introduce nanometre-sized pores by phase separation into polymer lean and polymer rich phases. Figure 22 shows the finalised manufactured foams with scanning electron microscopy (SEM) (annealed at 150 ºC). The connectivity of the pores is visible, along with the presence of both micro- and nano-pores.

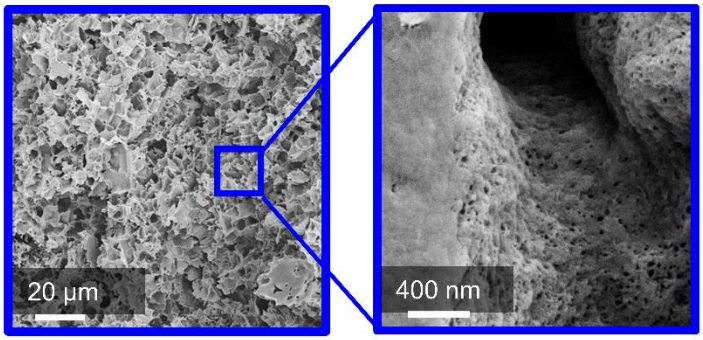

***Figure 22**. SEM microscopy images of the P3HT foam after annealing for 30 min at 150 °C. Reproduced with permission by John Wiley and Sons.*[32]

Figure 23 depicts schematically the fabrication of P3HT polymer foams. In brief, a highly concentrated solution of P3HT and ortho-dichlorobenzene (oDCB) was made and heated above the phase separation temperature of the system (100 ºC was used). A thick paste of P3HT resulted, to which salt was added, and after thorough mechanical mixing followed by slow cooling, a polymer-rich phase and a polymer-lean phase was formed with interconnected pores. The salt crystals and oDCB were removed over several days using a 1:9 water:methanol mixture.

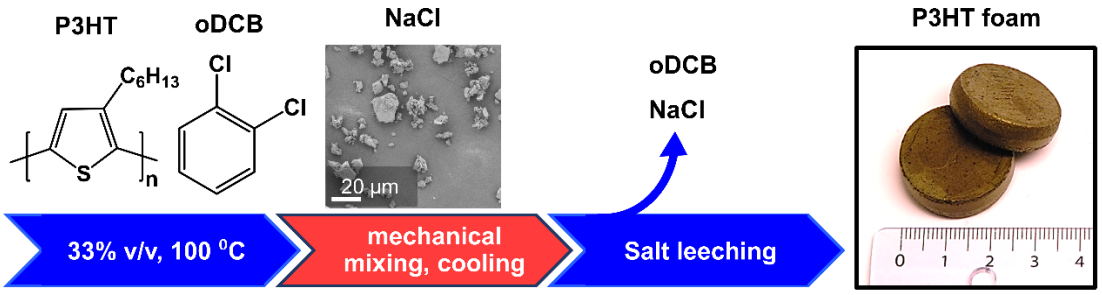

***Figure 23**. Flow chart of salt-leaching method for P3HT foam fabrication. Reproduced with permission by John Wiley and Sons.*[32]

The foams were doped using a sequential immersion method in a F4TCNQ-acetonitrile/dichloromethane solvent mixture. The quantity of F4TCNQ added to the foam

was followed using the weight increase of the foam over time (figure 24). As previously discussed, a key concept towards the use of polymer foams, c.f. to bulk solid, is the ready inclusion of dopant into the material. Figure 24 shows the superior uptake of dopant when compared to bulk material. Especially, the fastest dopant uptake is noted in the first four hours, concluding that a foam material is favourable in regard to dopant uptake for time conservation; and in fact, reaches a higher overall level of doping at all time steps shown for the same dopant concentration. Doping could be further accelerated by increasing the concentration of the dopant.

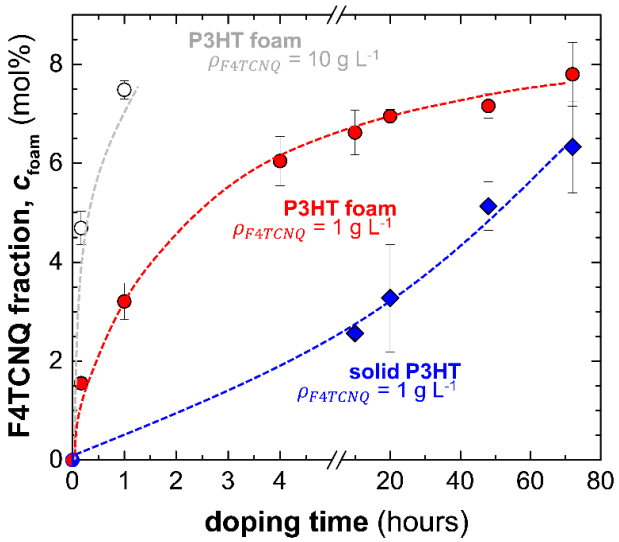

***Figure 24**. Uptake of F4TCNQ in mol% as function of doping time for foam (red circles) and solid samples (blue diamonds) for low concentration of the dopant solution, and for foams doped with high concentration of the dopant solution (white circles). Dashed lines are a guide to the eye. Sample dimensions: l × w × h, weight are ≈ 10 mm × 1.5 mm × 1.5 mm, 10 mg for foams and ≈ 10 mm × 1.5 mm × 0.4 mm, 5 mg for films. Reproduced with permission by John Wiley and Sons.*[32]

4.2 Electrical and Thermal Measurements

Once the foams were manufactured, electrical and thermal characterisation were performed. Electrical characterisation was performed in turns with Dr Kroon, and thermal characterisation by myself.

Electrical characterisations

Electrical conductivity, σ, measurements were performed using a two-point-probe setup (Keithley 2400 sourcemeter) for all foams and a four-point-probe setup (Jandel, model RM3000) for all films. Contact resistance in the two-point-probe setup was discounted after performing a contact resistance test by plotting sample length vs resistance and attaining a linear relationship. Measured films were 5 µm thick, as thicker samples (400 µm) were difficult to dope and led to cracked samples during doping. Due to an increased tortuosity (an increased path length for electrons to travel between electrodes due to the presence of pores preventing the shortest and straightest path being taken),[79,80] and the presence of a large air content, a decrease in σ was expected for foamed material c.f. bulk material, this was proven by the measurements undertaken, with bulk material attaining a maximum average σ = 3.5 S cm^{-1}, whereas foams displayed σ = 0.2 S cm^{-1} (samples doped in one step).

Seebeck coefficients, α, were determined experimentally with a SB1000 Seebeck unit (MMR technologies), where the samples were not reused after characterisation. The Seebeck coefficient is not effected by foaming P3HT, since air has a very low negligible electrical conductivity of $\sigma = 10^{-14} – 10^{-15}$ S cm^{-1}, and therefore the pores do not contribute to the Seebeck coefficient. Hence, the Seebeck value is expressed purely as that of the polymer. Maximum values for bulk and foamed materials were α = 52 µV K^{-1} and 67 µV K^{-1} respectively (for the above reported σ values).

Figure 25 shows the comparison between bulk and foamed material at several different doping times and concentrations. σ and α follow a power law relationship;[9] the trend lines are shifted since the measured films possess a higher conductivity c.f. the foams. Doping foam samples with either a dopant concentration of 10 g L^{-1} for one hour or 1 g L^{-1} for four hours resulted in the same measured values of σ and α, which is supported by figure 25 showing the similar dopant uptake for the afore mentioned concentrations and times.

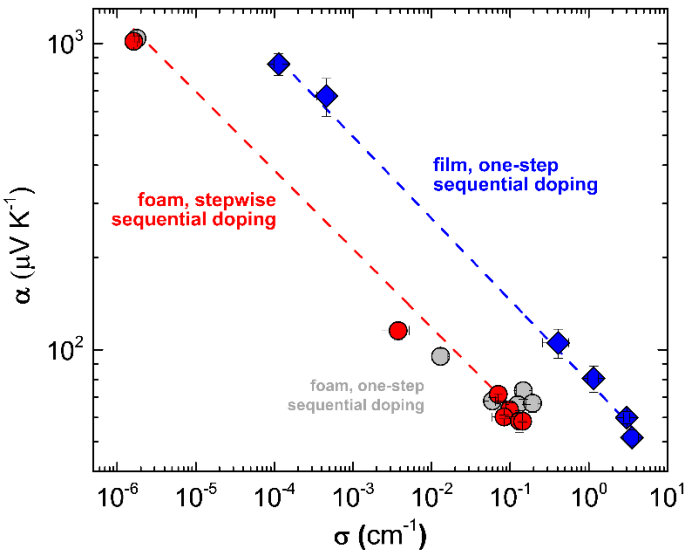

Figure 25. *Logarithmic plot of Seebeck coefficient α as function of electrical conductivity σ of P3HT foams and films after immersion doping with F4TCNQ: foam samples (l × w × h ≈ 10 mm × 1.5 mm × 1.5 mm) stepwise sequentially doped with 4% F4TCNQ for 20 h per doping step (red circles) or in one step (grey circles) with varying dopant concentration (1 or 10 g L^{-1}) and doping times (10 min, 1 h or 4 h); solid 5 µm thick dropcast P3HT films sequentially doped for 24 h (0.005, 0.01, 0.05, 0.1, 0.5, and 1 g L^{-1}). Reproduced with permission by John Wiley and Sons.*[32]

Theoretically one can determine the conductivity of a foamed conducting polymer based upon the values one attains for a solid conducting sample. Equation 14, which is based on effective medium theory,[81,82] is taken to calculate the relative difference factor, σ_r, between a film and a foam, with V_p = 0.66 for the porosity of our foam (calculated from the 66% porosity of the manufactured foams), and n = 1.5 (n = shape factor for spherical pores) giving a dimensionless correction value of σ_r = 0.19.

$$\sigma_r = (1 - V_p)^n \qquad \text{(eq. 14)}$$

Using the correction factor, σ_r = 0.19, the foams theoretically should possess σ = 0.7 S cm^{-1}, a factor of 5 lower than their parent solid film, whereas experimentally, the P3HT foams attain 0.2 S cm^{-1}, just over an order of magnitude lower, which is most likely due to an underestimate of the tortuosity in the calculation of σ_r.

Thermal conductivity

Thermal conductivity, κ, measurements were undertaken with a TPS250 setup (HotDisk). A key redeeming factor, in terms of absolute thermoelectric performance is the fact that a foam is comprised of air as well as polymer material, meaning it will have a lower thermal conductivity than a solid polymer sample. Samples of solid P3HT (doped and undoped) were pressed from powder into pellets at room temperature, followed by pressing at 80 and 150 ºC respectively, to ensure a fully compact material. First, an anisotropic analysis was undertaken, confirming the samples were all isotropic, therefore an isotropic analysis method was used for all samples (see Chapter 2.1.3 for details on methodologies).

Solid samples for undoped and doped P3HT possessed near identical thermal conductivities of 0.34 ± 0.01 and 0.32 ± 0.01 W m^{-1} K^{-1} respectively, which is attributed to the low electrical conductivity of the samples (a small $\kappa_{electronic}$ contribution in the order of 10^{-3} W m^{-1} K^{-1} arises from the low σ of the foams – see Chapter 2.1.3 for κ contributing factors). Using the rule of mixtures an estimate of the thermal conductivity for foams can be made (equation 15).

$$\kappa_{foam} = \kappa_{P3HT}\left(1 - \frac{p}{100}\right) + \kappa_{air}\frac{p}{100} \qquad \text{(eq. 15)}$$

Thermal conductivities of κ_{P3HT} = 0.32 W m^{-1} K^{-1} (measured value) and $\kappa_{air} \approx 0.025$ W m^{-1} K^{-1} (known value), with porosity, p = 66, lead to a theoretical value of $\kappa_{foam} \approx 0.12$ W m^{-1} K^{-1}, which is in close agreement to the measured value of 0.14 W m^{-1} K^{-1}.

4.3 Foam Properties

In order to compare the different materials, bulk and foamed P3HT, the figure of merit, *ZT*, was calculated at T = 300 K. For doped foams a $ZT \approx 2 \times 10^{-4}$ is calculated. In order to accurately compare the foamed and solid materials for the same doping level, the same Seebeck value was used for both calculations. For the *ZT* of the foam the data points from a measured sample were used, with α = 67 µW K^{-1}, corresponding to σ = 0.2 S cm^{-1}. Thus, α = 67 µW K^{-1} for the bulk material was selected and the trend line from figure 25 was used to extrapolate σ = 1.8 S cm^{-1} to give a $ZT = 8 \times 10^{-4}$. If the maximum attained thermoelectric parameters are used, rather than the average, the bulk material and foam attain

a figure of merit of $ZT = 1 \times 10^{-3}$ and 2.3×10^{-4}, respectively, which is the same ratio as when the average values are used to calculate the *ZT*.

The lower thermoelectric performance of the foams c.f. solid material, can be ascribed to the lower electrical conductivity attained (due to the large air content present in the foams), which is not fully compensated for by its lower thermal conductivity. A modified *ZT* can be used, *ZT'* (equation 16), which takes into account the actual amount of material used to produce the thermoelectric material.

$$ZT' = \frac{\alpha^2 \sigma}{\kappa} T \cdot \frac{100}{100 - p} \qquad \text{(eq. 16)}$$

ZT is thus adjusted for a fair comparison of the amount of material used, to the similar values of $ZT' = 6$ and 8×10^{-4} for foam and bulk, respectively. Taking into account the *ZT'*, it is concluded that the overall thermoelectric performance of a set amount of material is not overly compromised when it is foamed. A distinct advantage is that the doping of the material is considerably faster allowing for optimal leg geometries to be doped and used even if they are required to be large, such as in cases where more material is needed to match the dimensions of p- and n-legs (see Chapter 2.2.1 for leg geometry optimisation). Further, the foam material could in fact have its thermal conductivity further altered by tuning the porosity of the material.

Chapter 5

CARBON NANOTUBE COMPOSITES WITH CONDUCTING POLYMERS

The use of nanocomposites, based upon the combination of carbon nanotubes (CNTs) and polymers, is an attractive strategy towards high-performance thermoelectric plastics. When formed, a nanocomposite can harness the attributes of the carbon nanotubes and the support matrix of the polymer, to attain a material electrically and mechanically superior to the individual components. Polymers that are used for thermoelectric purposes tend to be brittle due to the large amount of dopant introduced to them in order to attain workable conductivities; pure CNTs can easily become airborne when not bound in a polymer matrix and, depending on their length, may pose a threat to the respiratory system.[83] Nanocomposites circumvent these issues by not using molecular dopants and entrapping the nanotubes in a polymer matrix.

Individual CNTs possess a high thermal conductivity, κ, ($\approx 10^3$ W m^{-1} K^{-1}),[84] however κ is lower in the case of a mesh of CNTs. Aliev *et al.*[85] attained $\kappa \approx 50$ W m^{-1} K^{-1} for a CNT mesh by purposely creating an oriented sample in an attempt to make a sample as highly thermally conducting as possible by measuring along the direction of CNT orientation. Lower values of κ are expected for isotropic films ($\kappa \approx 26$ W m^{-1} K^{-1}).[86] The significantly lower values of κ for pure CNT films c.f. single CNTs can occur due to effects such as: contact resistance at the tube-tube interfaces, from quenching of phonons in aggregated CNT bundles, and radial heat loss perpendicular to the direction of measurement.[84] The κ value for CNTs is also lowered in CNT:polymer nanocomposites due to the same reasons as in pure CNT films, however the interfacial thermal resistance between CNT and polymer (arising from phonon scattering) and the spatial separation of CNTs (i.e. regions of no contact between some CNTs) are additional effects, resulting in thermal conductivities of no more than a few W m^{-1} K^{-1} for an isotropic nanocomposite.[87]

CNT nanocomposites are usually manufactured via the addition of carbon nanotubes to a polymer, followed by exfoliation of the carbon nanotubes by shear. They are often

solution processed, but they can also be processed in the melt,[88] for example, in an extruder. Current literature for state-of-the-art materials are summarised in two recent reviews by Blackburn *et al*. and Yao *et al*.[38,58] A System of particular note is that of Sarabia *et al*.[63] who used polyvinylpyrrolidone (PVP) to alter the majority charge carrier of MWNTs from holes to electrons in films, the thermoelectric properties of which are displayed in table 1. Together in collaboration with Sarabia *et al*., this system was used as the main 'ink' for coating PET yarn in Paper IV (see Chapter 6.2). Nanocomposites are proving to be a popular and well-studied type of thermoelectric material; table 1 displays a sampling of several different material combinations and the years of their publication.

	Polymer	Filler	Electrical conductivity (S cm^{-1})	Seebeck coefficient (μV K^{-1})	Power factor (μW m^{-1} K^{-2})	Year	Reference
p-type	PEDOT:PSS	SWNTs	1350	59	464	2017	89
	PEDOT:PSS	Te nanowires	115	215	284	2016	90
	PEDOT:PSS	DWNTs	780	43.7	151	2016	91
	PEDOT:PSS + PaNi	DWNTs + graphene	1885	120	2710	2016	92
	PaNi	SWNTs + Au NPs	1106	150.86	2454	2016	93
	P3HT	SWNTs	2760	31.1	267	2015	94
	PEDOT:PSS	DWNTs + TCPP	960	70	500	2013	95
	PEDOT:PSS	SWNTs	3300	20	140	2013	96
	PEDOT:PSS	Te nanowires	11	180	35	2013	97
	PEDOT:PSS + PVAc	SWNTs	950	41	160	2011	98
	PaNi	MWNTs	61.47	28.6	5	2010	99
	PEDOT:PSS	Te nanowires	19.3	163	70.9	2010	100
n-type	PVP	MWNTs*	30	-15	0.7	2017	63
	PEG	SWNTs	0.2	-56	0.06	2017	101
	P3HT	MWNTs	1	-10	0.01	2016	62
	PEI	SWNTs	39	-63	15	2014	102
	PVP	SWNTs	33.3	-53	9	2013	60
	pVpY	SWNTs	27.2	-47	6	2013	60
	PEI	SWNTs + $NaBH_4$	≈50	-80	≈32	2012	103

Table 1. A sampling of polymer:filler thermoelectric materials with electrical conductivity, Seebeck coefficients and power factors. Sorted by majority charge carrier type and year of publication. Meanings for abbreviations found in nomenclature section of this thesis (p.ii). *20 wt% CNTs, as used in Paper IV work.

In the case of Paper II, all nanocomposites were prepared by dispersing nitrogen doped, n-type multi-walled CNTs (N-MWNTs)[104] in orthodichlorobenzene (oDCB) with a sonic bath, followed by addition in parts of poly(3-hexylthiophene) (P3HT) dissolved in chloroform, to the N-MWNTs with further bath sonication. Films were made by drop-casting the nanocomposite solution onto polyethylene terephthalate (PET) foil as a substrate.

Two types of N-MWNT were used; 'as synthesised' nanotubes with a remnant of iron from synthesis, and acid-treated nanotubes with most of the iron removed. The N-MWNT's were synthesised by Qian *et al.*[104] by chemical vapour deposition in a nitrogen carrier gas, from acetonitrile-ferrocene mixtures, in a scaled up process demonstrated previously by Jacques *et al.*[105,106] Either way the N-MWNTs possessed n-type character with Seebeck coefficients, α, of ≈ -10 μV K^{-1}. When combined with P3HT, as in the above mentioned process, systems with both N-MWNT types possessed a percolation threshold, c^*, of ≈ 3.5 wt% (see Chapter 5.1, *Electrical conductivity* for more detail). In the case of the 'as synthesised' carbon nanotubes, a novel switching behaviour between p-type and n-type was observed related to N-MWNT content, with a switching concentration, c_s, of ≈ 40 wt% (p-type < 40 wt%, n-type > 40 wt%) (figure 26).

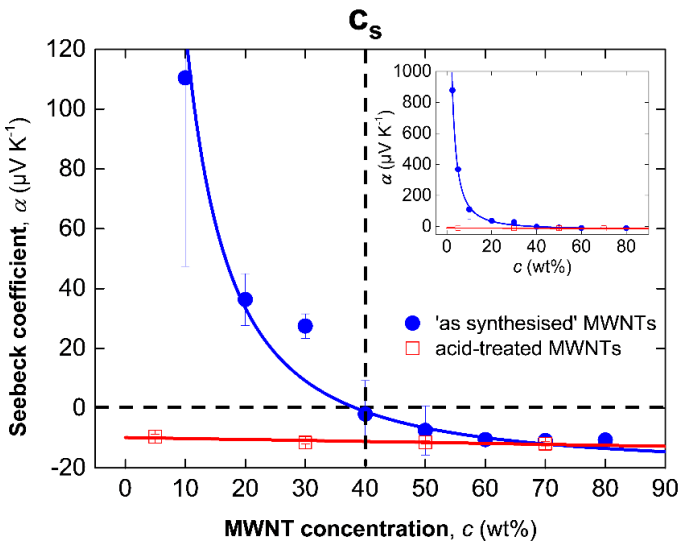

Figure 26. *α steadily decreases with increasing CNT concentration, and crosses over to negative values at c_s = 40 wt% CNTs. For higher CNT concentrations, α saturates at about -10 μV K^{-1}. For the acid-treated CNTs, α is independent of the CNT concentration in the investigated range. The inset shows the complete measured composition range. Data reproduced with permission by John Wiley and Sons.*[62]

The charge transport in the 'as synthesised' nanocomposite takes place via the percolated nanotubes (as the more conducting component), in the case of c_s < 40 wt% the majority transport carriers are holes, as the P3HT is thought to dope the nanotubes, whilst c_s > 40 wt% the majority transport carriers are electrons, a result of excess negative charge from the nitrogen present in the N-MWNTs. The hypothesis that P3HT is in fact doping the N-MWNTs is supported by photoluminescence (PL) experiments (performed by Dr Bernhard Dörling, ICMAB – see Paper II, figure 3b), where the addition of N-MWNTs causes PL quenching of the P3HT, which is also discussed in the work of Stranks *et al*. who demonstrated PL quenching in a charge transferring system of single-walled CNTs with P3HT.[107] Acid-treated N-MWNTs conversely undergo a far lower interaction with P3HT c.f. 'as synthesised' N-MWNTs, which is also shown in Paper II, figure 2d with a reduced P3HT PL quenching, thus a less effective p-doping of the N-MWNTs, which gives rise to the n-type character of the acid-treated N-MWNT:P3HT nanocomposites at all nanotube weight percentages above *c**.

5.1 Electrical and Thermal Measurements

Electrical conductivity

Electrical measurements were performed upon films with a 4-point van der Pauw method as described in Chapter 2.1.2 of this thesis. Electrical conductivity, σ, varies in relation to the N-MWNT content; in the case of acid-treated N-MWNTs, σ increases with increasing N-MWNT content, as seen in figure 27, which is an expected increase with the limited interaction and p-doping with and from P3HT, as discussed previously at the start of this chapter. However, the 'as synthesised' N-MWNTs possess a less straight forward relationship; initially the trend is the same as for the acid-treated N-MWNTs, an increasing nanotube content leads to an increase in σ, followed by a drop in σ at the switching point between p- and n-type.

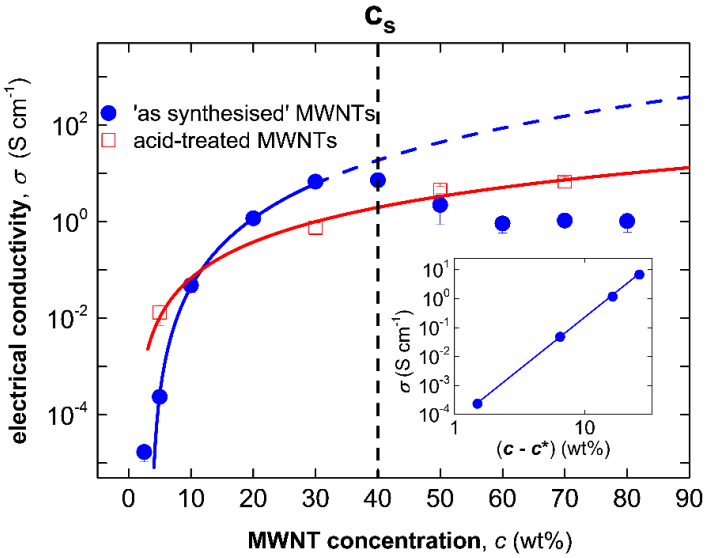

***Figure 27**. σ shows percolative behaviour, increasing by several orders of magnitude upon addition of a few wt% of CNTs. At high CNT content, a dip in σ is observed for as-synthesized CNTs. The dashed line sketches the expected behaviour for similar composites prepared from regular, undoped CNTs. Data reproduced with permission by John Wiley and Sons.*[62]

The initial increase in electrical conductivity following c* is rather sharp, then levels off until c_s, which is typical for a percolating system. Generally, the increase in electrical conductivity can be attributed to the addition of hole charge carriers by doping of the N-MWNTs with P3HT. However, with increasing N-MWNT weight percentage and thus a lower P3HT content (hence less p-doping), the n-type character from the nanotubes begins to prevail leading up to c_s, resulting in a slight plateau. The drop in conductivity after c_s can be ascribed to the switch in majority charge carrier type (from holes to electrons), where the p-doping from P3HT is no longer dominating, resulting in an initially lower amount of charge carriers, thus lower σ. As the N-MWNT content is further increased after c_s, a slight increase in σ is measureable as the charge carrier concentration is increased, as the nanocomposite reaches the σ of neat nanotubes.

The inset in figure 27 shows a linearised plot of electrical conductivity vs. corrected wt% ($c - c^*$) which takes into account data above the percolation threshold but before the switching point of p- to n-type.[108] The data is plotted on a log-log scale in order to assess how closely the data adheres to the power law $\sigma \propto (c - c^*)^{\beta}$, where β is the critical exponent,

the gradient of the fitted line. The data in fact appears to fit the power law well, and percolating behaviour can be confirmed.

Seebeck coefficient

Seebeck measurements were performed in duplicate in most cases, with one set of data from a custom setup performed by Dr Dörling, and the other by myself with a SB1000 setup from MMR technologies, USA, as described in Chapter 2.1.1 of this thesis. The Seebeck coefficient is arguably the most important factor of the study in Paper II, where it can be switched between p- and n-type with both N-MWNT concentration variation and by applying UV light to the system.

Thermal conductivity

All thermal conductivity, κ, measurements were performed by myself using a TPS250 setup from HotDisk, Sweden, upon 1 mm thick samples, using an isotropic method (see Chapter 2.1.3 for details on methodologies). Given the high κ of CNTs, measuring the thermal conductivity of the produced nanocomposites was valuable in order to accurately describe their performance and to avoid a misrepresentation of data (since polymers are known to have a low κ, *PF*s could be confidently used in cases where CNTs are not used – see Chapter 3 for examples).

Values of κ were determined for a panel of some of the fabricated nanocomposites, summarised in table 2 along with values for density, specific heat and thermal diffusivity for the measured samples. Due to the large amount of material required to measure each composition, it was not possible to measure κ for each composition discussed in Paper II.

N-MWNT content	Density ρ_d (g cm^{-3})	Specific heat C_p (J kg^{-1} K^{-1})	Thermal diffusivity D (mm^2 s^{-1})	Thermal conductivity κ (W m^{-1} K^{-1})
neat P3HT	1.05 ± 0.01	1497 ± 15	0.18 ± 0	0.29 ± 0.01
30 wt%	1.13 ± 0.01	1234 ± 4	0.29 ± 0	0.40 ± 0.03
30 wt% acid-treated	1.17 ± 0.01	1194 ± 2	0.35 ± 0.01	0.49 ± 0.02
80 wt%	1.21 ± 0.01	948 ± 2	0.48 ± 0.01	0.55 ± 0.04

***Table 2**. Measured properties used to determine the bulk thermal conductivity κ of 1 mm thick P3HT-CNT samples. Data reproduced with permission by John Wiley and Sons.*[62]

It is of particular note that the values of κ do not change dramatically with increased N-MWNT content, this can be attributed, as discussed previously, to the ability of the matrix polymer, in this case P3HT, to mitigate the high κ of the nanotubes. The values for 80 wt% N-MWNT are only approximately twice that of neat P3HT, which is still 2 orders of magnitude lower than that for pure CNT films, as measured by Lian *et al*. and Duzynska *et al*.[86,109]

5.2 UV Switching from p- to n-type

The ability to switch the majority charge carrier of a nanocomposite by way of concentration manipulation is a useful tool. To further utilise a switchable system in a practical way, it would be advantageous to switch a system from p- to n-type (or vice versa) from a single solution or ink, in this way excessive processing would not be required. Additionally to the concentration manipulation switching, demonstrated in Paper II is the switching of the overall p-type character expressed from the interaction between the matrix polymer P3HT and the 'as synthesised' N-MWNTs, to overall n-type. Two different methodologies were investigated to switch a single nanocomposite solution between p- and n-type, both relying upon disruption of the interaction between the N-MWNTs and the p-type P3HT. Firstly, heat was applied to a still wet drop-casted sample of 30 wt% to attempt to reverse the crystallisation and wrapping of the P3HT to and around the N-MWNTs, resulting in a more orange/brown solution indicating dissociation of the nanotubes; unfortunately this change was apparently reversible and did not remain after drop-casting, and instead resulted in films that possessed no change in character (at lower used temperatures < 120 ºC), or in films with a dramatic increase in resistance and no switching in Seebeck coefficient (for higher temperatures > 120 ºC).

Ultimately, UV light treatment (at 50 mW cm^{-2}) was selected and performed by Dr Dörling with the intention to irreversibly degrade the conjugation in the P3HT polymer to allow for full expression of the N-MWNTs Seebeck coefficient by preventing p-type doping. Given the short penetration depth of UV light, attempts made upon dried films were unsuccessful in altering the entire material to n-type. However, when performed upon dilute solutions of concentrations ≈ 1 g L^{-1}, UV light treatment was successful in degrading the P3HT as the negative α of the N-MWNTs was measured once the films were dried (≈ -10

μV K^{-1}). During the drying of the films, a natural convection together with a relatively clear solution allowed for full effect of the UV light upon the drying solutions. Figure 28 follows α with applied UV treatment time on 20 wt % and 30 wt% samples of acid-treated N-MWNT:P3HT nanocomposites. Longer UV treatment times lead to greater disruption of the interaction between the N-MWNTs and P3HT via degradation of the polymer's conjugation. Over time, the 20 wt% nanocomposite sample is unable to achieve n-type character, however the 30 wt% sample, given its lower initial α value, is able to become n-type overall.

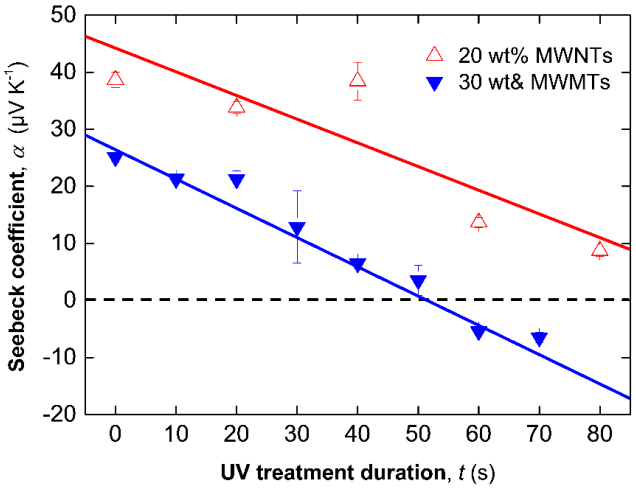

***Figure 28**. Dependence of Seebeck coefficient on UV treatment duration for 20 wt% (red open triangles) and 30 wt% samples (filled blue circles). Data reproduced with permission by John Wiley and Sons.*[62]

As with N-MWNT wt% variation, σ is also affected by the applied UV light. As UV light is applied to the system, and degradation of the P3HT occurs, the overall σ of the nanocomposite decreases (figure 29). These measurements were performed by Dr Dörling at ICMAB, Barcelona. The degradation of P3HT will lead to a lowered p-doping of the nanotubes (hence why the switching occurs with applied UV light), but because of this process, the nanotubes will then possess a lower charge carrier concentration, thus a reduced σ. Even though the N-MWNTs are percolated, the P3HT can behave as a junction material, bridging gaps between nanotubes, and if the P3HT between nanotubes is degraded, and no longer conductive, this will also contribute towards a lower σ for the system, as the nanotubes are no longer electrically connected.

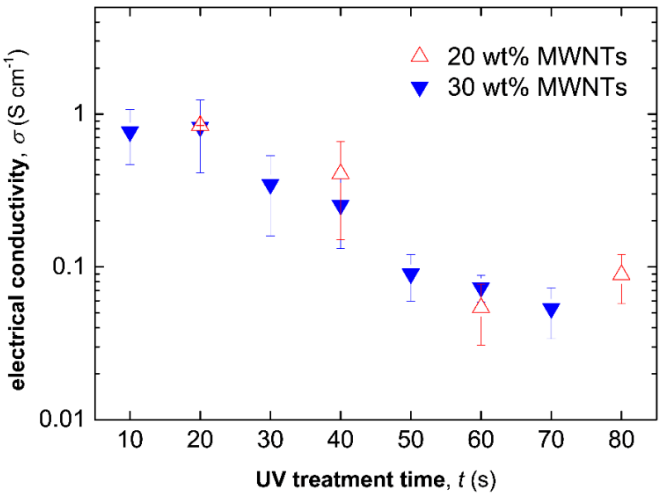

***Figure 29**. Dependence of electrical conductivity on UV treatment duration for 20 wt% (red open triangles) and 30 wt% samples (filled blue circles). Data reproduced with permission by John Wiley and Sons.*[62]

5.2.1 Thermoelectric Module

A prototype module was constructed by Dr Dörling using a 30 wt% single 'ink' solution of 'as synthesised' N-MWNT with P3HT, taking advantage of the UV switchable behaviour to create p- and n- legs. Following the schematic in figure 30a-d; first, the solution was drop-cast onto a PET foil. Then half was masked, and while still wet, the solution was irradiated with UV light (figure 30a). Second, the sample was cut into strips and the interface between the p- and now n-type areas had silver paste applied (figure 30b). The film was then folded as shown in figure 30c-d, in order to create an out-of-plane thermoelectric module.

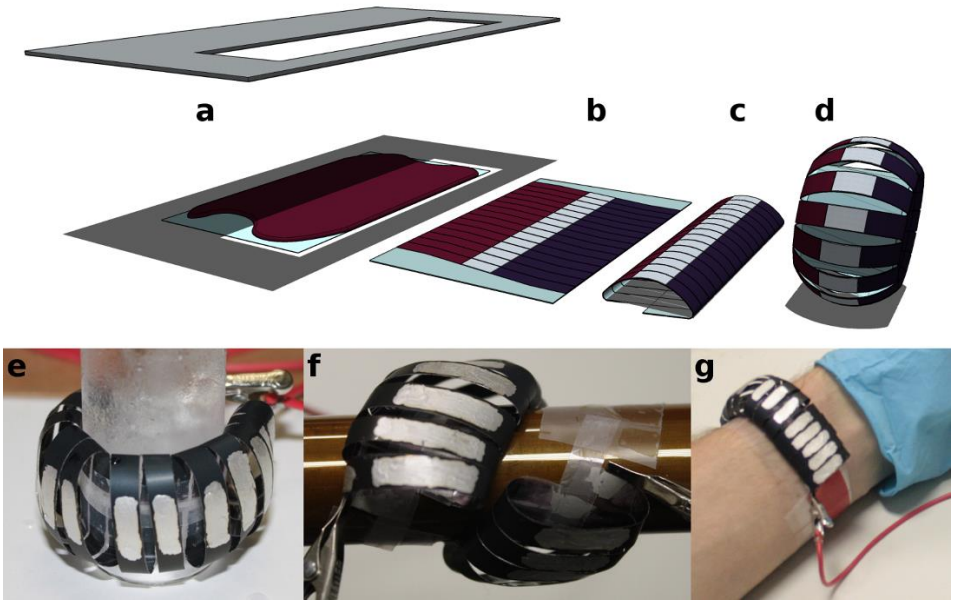

***Figure 30**. Proposed fabrication and applications of a device geometry that plays on the advantages of the presented material. a) A large area is coated from a single solution, and patterned by UV irradiation. b) If desired, additional contacts (on what will be the outer side) are deposited. c) The flexibility of the PET substrate is employed to easily connect the couples electrically in series by depositing contacts at what will be the inner side of the torus. d) The final toroidal device geometry. Possible application geometries in the form of e) a single torus, f) an extended spiral, and g) a wristband. The width of a single leg of the pictured device is 5 mm. Reproduced with permission by John Wiley and Sons.*[62]

The module can be used in several conformations; a single torus (figure 30e), an extended spiral (figure 30f) and a wearable wristband (figure 30g). The module consisted of 15 legs, where the width of each leg is 5 mm. The thermoelectric module was characterised by attaching the module to a glass of ice water as a cold sink, and the other side left at room temperature as the hot sink. The module generated a voltage of 5 mV, corresponding to a total 217 µV K^{-1} for the module, or 14.5 µV K^{-1} per leg. Characterisation of the output power at load matching conditions gave rise to a current ≈ 2 nA, at a temperature difference of 23 K.

It is expected that this methodology of switching will be applicable to other systems, so with that in mind, a selection of better performing materials, like semiconducting single-walled CNTs and appropriate dopants,[110] coupled with processing methods such as vapour printing,[111] along with UV light switching, could lead to high performing modules.

4.3 Nanocomposite Thermoelectric Properties

The nanocomposites in Paper II can be characterised by a high degree ambient electrical stability, with n-type samples showing no significant change in α over 34 weeks. Further, values of σ decreased by no more than half of their initial value, and remained stable in measurements made after 85 weeks.

Referring to Chapter 2.1.4, equation 10, of this thesis, the figure of merit can be defined as $ZT = (\alpha^2\sigma/\kappa)T$. The non-optimised *ZT* for the p-type material is around 10^{-3} and for the n-type is around 10^{-5} (the n-type material was calculated from 80 wt% N-MWNTs - κ was not determined for UV irradiated samples). The attained n-type *ZT* could be considered as low, although the *PF*s for other recent n-type materials (around 0.1-2 μW m^{-1} K^{-2})[63,112,113] are only an order of magnitude larger than the here attained *PF* of 0.01 μW m^{-1} K^{-2}.

Chapter 6

ELECTRONIC AND THERMOELECTRIC TEXTILES

Textiles feature as a constant part of our day-to-day life, they are flexible, and can be found in clothing, furniture, automobiles and medical bandaging. Since textiles are so wide spread and commonplace, a promising and potentially useful avenue of exploration would be to infuse them with electronic functionalities. Upon successful integration, the resulting electronic textiles (e-textiles) could offer application in several areas from medical care[114,115] to energy harvesting and storage.[116-119] An essential component towards the realisation of e-textiles is the development of conducting fibres. A multitude of conducting fibres currently exist, with most created to satisfy different purposes, for example: photovoltaics,[117,120-122] piezoelectrics,[123,124] triboelectrics,[118,120,125] thermoelectrics,[20,21,126,127] and also as conductive "wires" for general electrical connection purposes.[21]

More generally, fibres reside in one of two categories, natural and synthetic. Natural fibres are based upon either cellulose (e.g. cotton) or protein (e.g. silk and wool), and in both cases these fibres are characterised with high molecular weights (for example: 1500 kg mol^{-1} for cotton) and a high degree of orientation along the fibre axis resulting from natural growth. In fact one of the toughest known fibres is a silk spun by a certain variety of spiders, where the toughness arises from a high molecular weight 600 kg mol^{-1}, hydrogen bonding and alignment.[29,128] Synthetic fibres were first reported in 1953 by Quig[129] and can be formed from such polymers as polyethylene terephthalate (PET), polyamide (PA), polyacrylonitrile (PAN) and polypropylene (PP). The molecular weight of the polymer is directly responsible for the determination of the mechanical properties and spinability of the system.

Fibres can be manufactured by fibre spinning, inspired in part by the biological actions of spiders and silkworms, where the animal will prepare in glands a spinnable liquid and then extrude the liquid which hardens in the form of a fibre.[130] Melt spinning is the most common synthetic fibre formation method, and can be summarised as taking a polymer melt that is rapidly pumped through a spinneret (or die) which can possess one or several holes, followed by the cooling and drawing of the filament(s) which are then collected on a bobbin.

Fibres can be used as a monofilament (e.g. fishing wire), but in many cases they will be spun into yarns via mechanical twisting of several fibres, which stay together through friction. In the case of the work in Paper III and Paper IV, both silk and PET were used in the form of yarns. Further, yarns can be made into textiles, where textiles is defined as any material which possesses fibres. This can be achieved by such methods as weaving or knitting to give the traditionally perceived flat 2D structure which one will see for example in woollen jumpers.

Conducting fibres can be realised in several ways, which can include the previously mentioned spinning to form bulk polymer fibres, which can then be doped (see Chapter 3.1.1 for doping). Examples of high performing systems of doped fibres include: polyacetylene doped with iodine to give electrical conductivities, σ, of 13,000 S cm^{-1},[131] with a more recent example using poly(3,4-ethylenedioxythiophene):poly(styrene sulfonate) (PEDOT:PSS) to attain σ = 2804 S cm^{-1}.[132] Additionally, spinning of nanocomposites offers a promising avenue towards bulk conducting fibres, attaining on average values of 0.1 S cm^{-1}. Nanocomposite fibres is a field that could be explored and expanded, with a notable work by Esrafilzadeh *et al*. documenting fibres produced with σ = 1.5 S cm^{-1}.[133] For a more complete overview, a recent review by Lund *et al*.[29] covers many systems, with their formation and properties.

Conducting fibres can also be realised from either coating or dyeing pre-existing natural or synthetic fibres. For example, one can take negatively charged polyelectrolytes, with the negative charge occurring from charged acetate or sulfonate groups, to physically bind to a fibre/yarn such as silk, where the silk will have a net positive charge at low pH (see Chapter 6.1.1). The use of charges is a common feature of acid dyes that are regularly used by the textile industry to colour natural fibres such as wool, mohair, and silk.[134] Some current literature examples include work by Lu e*t al*. who attain fibres with reduced graphene oxide on silk with conductivities of 36 S cm^{-1}.[135]

6.1 p-type Yarns

One significant component of a fully functioning thermoelectric textile module are conducting p-type fibres or yarns. The work undertaken in Paper III focused upon the dyeing of silk with PEDOT:PSS to attain mechanically robust, machine-washable, p-type yarns for

use as conducting "wires" and for textile thermoelectrics. Further, since PEDOT:PSS and silk are both biocompatible, a system incorporating both of these components could be safely used with human contact.

6.1.1 Manufacture

Initial investigations included a screening of different methods for dyeing silk yarn (sourced from Bombyx mori silk worm cocoons) with the polymers PEDOT:PSS or the self-doping poly(4-(2,3-dihydrothieno[3,4-b]-[1,4]dioxin-2-yl-methoxy)-1-butanesulfonic acid (PEDOT-S)[136] (figure 32). In the case of PEDOT:PSS, either dimethyl sulfoxide (DMSO), ethylene glycol (EG) or methanol (MeOH) were added to enhance the electrical conductivity (see Chapter 3.2.1). In all cases the ability for silk to undergo a switching of net charge, depending upon the pH of the dying solution (figure 31), was utilised to allow it to be dyed. The isoelectric point of silk is approximately at pH 4,[137] meaning the yarn will possess a net positive charge in sufficiently acidic conditions. Both PEDOT:PSS and PEDOT-S possess sulfonate groups in aqueous media, which given the low p*K*a < 0 of sulfonic acids, will still be dissociated even at low pH, leading to a negative charge on the $–SO_3H$ groups of PEDOT-S and PSS of PEDOT:PSS.

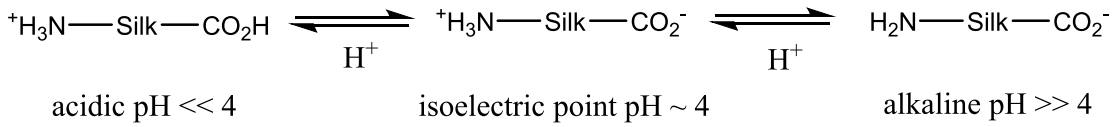

***Figure 31**. Net charge of silk below (left), at (middle), and above (right) it's isoelectric point.*

PEDOT:PSS water suspensions have a ≈ pH 2, allowing for direct use without pH tuning, unlike PEDOT-S where the pH was tuned to pH 1 with hydrochloric acid (HCl). pH 1 was selected for the PEDOT-S system after a screening of several different pHs where pH 1 gave a higher electrical conductivity c.f. higher pHs. Originally, experiments focused upon the use of PEDOT-S, with the intention that its negative sulfonate functional group could bind to the positively charged silk (once adjusted with HCl). The PEDOT-S did in fact appear to bind to the silk, however, due to (relatively) poor thermoelectric properties, further detailed experiments were put on hold in lieu of a system with more potential, namely that of PEDOT:PSS.

First attempts to dye silk with PEDOT:PSS were focused on attaching as much polymeric material to the silk as possible. For example, the silk was submerged in a polymer solution under heat which then concentrated and essentially dried onto the silk, creating a very thick layer of material. Logically this would lead to a lower electrical resistance following that more conducting material is present, however, as soon as the coated silk was slightly manipulated, the coating cracked and led to regions of high electrical resistance and areas of no electrical conductivity at all. A more measured approach was taken to attach less material, by drip coating the yarns with the polymer solution (running the solution along the yarn) followed by drying in air or with a heat gun whilst hanging vertically, with light weights on the yarns keeping them taught. Unfortunately, this method yielded high electrically resistive yarns, most likely again due to drying in a rigid strained position, which produced cracks and fissures in the conducting material once manipulated. So far the methods explored focused more on coating (with the expectation that some dyeing would occur), thus with the given results so far, a pure dyeing approach was taken, relying upon the negative charge from the sulfonic acid group to bind to the net positively charged silk. From the outcomes of the previously explored methods, exhaust dyeing (submersion of the silk which takes up polymer from a solution) was chosen. The silk was taken dry (with the prediction that if the silk was pre-wetted, an exchange of the water in the silk and the polymeric ink solution would have to first take place) and submerged in the aqueous PEDOT:PSS solution at pH ≈ 2 twice for one hour periods with bath sonication (Figure 32).

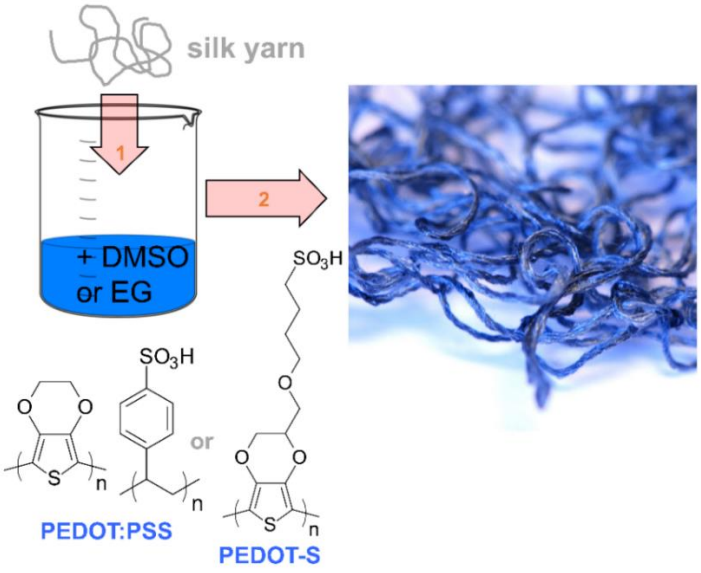

***Figure 32**. Schematic of silk dying with either PEDOT:PSS or PEDOT-S.*

Further, this successful exhaust dyeing methodology was repeated with cotton as the substrate, giving rise to weak yarns, most likely due to acid hydrolysis of the cotton. To attempt to alleviate acid hydrolysis, PEDOT:PSS solution was first neutralised with ammonium hydroxide giving rise to coated cotton yarns of comparable strength to neat cotton. For completion PEDOT:PSS was again neutralised with ammonium hydroxide and applied to silk to measure if a lack of acidic environment would have an effect on the mechanical properties of the PEDOT:PSS silk yarn.

6.1.2 Properties

Electrical and Mechanical

Electrical conductivity, σ, measurements were undertaken with a 2-point-probe system, given the fibre type geometries of the samples, with a Keithley sourcemeter. The samples were mounted onto a glass slide, taped at the ends, with silver paste applied along the yarn every 1 cm (overall 5 cm long segments). Several samples were measured for each material type, and in some cases up to 75 samples were measured ensuring a reliable and accurate reporting of data. Seebeck coefficients, α, were determined with a SB1000 unit from MMR Technologies, USA, by mounting samples on sample holders and measuring against a reference. All σ measurements take into account the insulating core of silk or cotton thus the values of σ are naturally lower than if only conducting material were taken into account. For long term stability measurements samples were left mounted on glass slides or sample holders for up to four months, with further measurements made ≈ 18 months after synthesis. Mechanical testing was undertaken with an Instron tensile tester (model 5565A) with 50 cm long samples with a cross head speed of 10 mm min^{-1}.

As discussed previously, the electrical properties for PEDOT-S dyed silk were low, for example the attained σ of PEDOT-S on silk was ≈ 3 x 10^{-2} S cm^{-1} whereas for films σ was found to be ≈ 1 S cm^{-1} (according to the original PEDOT-S work of Karlsson *et al*.).[136] For completion the Seebeck coefficient, α, of the PEDOT-S dyed silk was determined to be 8 μV K^{-1}, agreeing with α measured from films by Wang *et al*.[138] Unfortunately, due to significantly lower amounts of available PEDOT-S material, films were not cast, and focus was first put onto getting a working silk system. When PEDOT-S silk was processed at pH 2 a lack of colouring of the yarn, along with an unmeasurably high electrical resistance,

showed that a significantly lower amount of material was present.[139] Mechanically via tensile testing, the PEDOT-S performed similarly to neat silk with little loss in modulus (table 3). Given the low performance of PEDOT-S dyed silk, all further focus was placed upon PEDOT:PSS based systems.

			mechanical properties				electrical properties			
yarn	coating	processing agent	S_{break} (MPa)	ε_{break} (%)	E (GPa)	n	σ (S cm^{-1})	n	α (μV K^{-1})	n
silk	-	-	157 ± 12	11 ± 1	3.2 ± 0.3	45	-	-	-	-
	PEDOT-S	-	93 ± 16	13 ± 1	2.4 ± 0.5	2	(3 ± 2)·10^{-2}	12	8 ± 1	2
	PEDOT:PSS	-	109 ± 31	8 ± 2	2.6 ± 0.5	3	(1 ± 1)·10^{-2}	15	18 ± 2	3
	PEDOT:PSS	EG	139 ± 22	12 ± 2	2.0 ± 0.2	21	15 ± 6	84	14 ± 1	4
	PEDOT:PSS	DMSO	136 ± 24	12 ± 3	1.8 ± 0.3	23	14 ± 4	84	15 ± 1	4
	PEDOT:PSS	MeOH	159 ± 20	12 ± 2	1.9 ± 0.2	18	14 ± 6	53	17 ± 3	4
cotton	-	-	305 ± 27	7 ± 1	5.3 ± 0.6	20	-	-	-	-
	PEDOT:PSS	EG	261 ± 35	6 ± 1	5.8 ± 1.8	8	12 ± 3	12	14 ± 1	2
	PEDOT:PSS	DMSO	260 ± 28	6 ± 1	7.0 ± 2.5	8	15 ± 6	18	14 ± 1	2
	PEDOT:PSS	MeOH	-[a]	-[a]	-[a]	-[a]	15 ± 4	18	16 ± 3	2

Table 3. *Mechanical and electrical properties of silk and cotton yarns dyed with PEDOT-S and PEDOT:PSS: stress at break, S_{break}, strain at break, ε_{break}, Young's modulus, E, electrical conductivity, σ, relative to the fiber cross section, and Seebeck coefficient α, measured for n yarn segments; [a]samples too brittle to be measured. Data reproduced with permission from the American Chemical Society.*[21]

Samples of PEDOT:PSS dyed silk, with different co-treatment methods (DMSO, EG, MeOH) were all measured extensively to attain electrical conductivities, Seebeck coefficients and values for mechanical characteristics. The different co-treatment methods yield samples with similar electrical properties. The samples of PEDOT:PSS with silk and cotton at pH 2 both average at $\sigma \approx 14$ S cm^{-1} and $\alpha \approx 15$ µV K^{-1} (irrespective of co-treatment method – see table 3 for more detail). The measured values for films of PEDOT:PSS with different treatment methods are: DMSO, $\sigma \approx 414$ S cm^{-1}; EG, $\sigma \approx 504$ S cm^{-1}; MeOH, $\sigma \approx 372$ S cm^{-1}. However, weight measurements show a polymer uptake to silk of ≈ 10 %, hence scaling for the amount of material on the yarn and using the film σ values, the yarns should be ≈ 45 S cm^{-1} on average between treatment methods. A lower than expected σ is likely to come from the rugged topology of the yarns and the microstructure differences compared to a thick film which is relatively smooth. During tensile testing, the samples based on silk (as with the PEDOT-S based materials) did not suffer much loss in Young's modulus and stress at break with almost identical elongation at break values, when comparing them to their untreated parent yarns (table 3). However samples based on cotton led to brittle samples, and in some cases (as with MeOH co-treatment) the samples were too brittle to be measured. Mechanical bending tests were implemented on silk/PEDOT:PSS samples to determine their electrical stability under practical use. A homemade Lego setup (figure 33, right) was used to repeatedly bend samples over a Teflon rod of either 52 or 4.5 mm diameter, by repeatedly lifting and reapplying a weight to the sample end. After 1000 cycles the electrical resistance increased by no more than 50 %, indicating a robust electrical performance (figure 33, left).

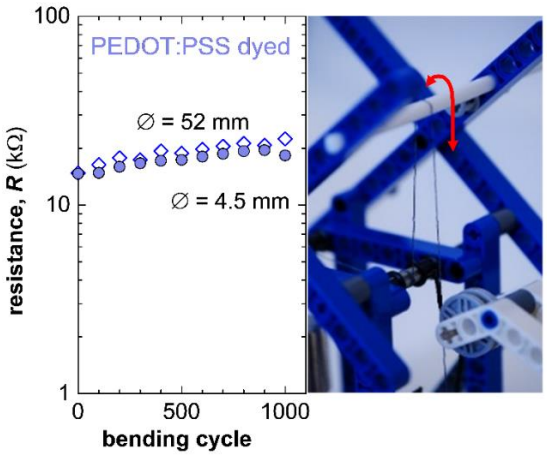

***Figure 33**. Resistance R of 32 cm long yarns bent repeatedly around Teflon bars with a diameter ⌀ of 4.5 (●) and 52 mm (◊). Reproduced with permission from the American Chemical Society.*[21]

Long term stability measurements of electrical resistance, *R*, (figure 34a) and α (figure 34b) show a tremendous degree of ambient stability, with measurements made as long as ≈ 18 months after synthesis, lending the material to practical everyday solutions.

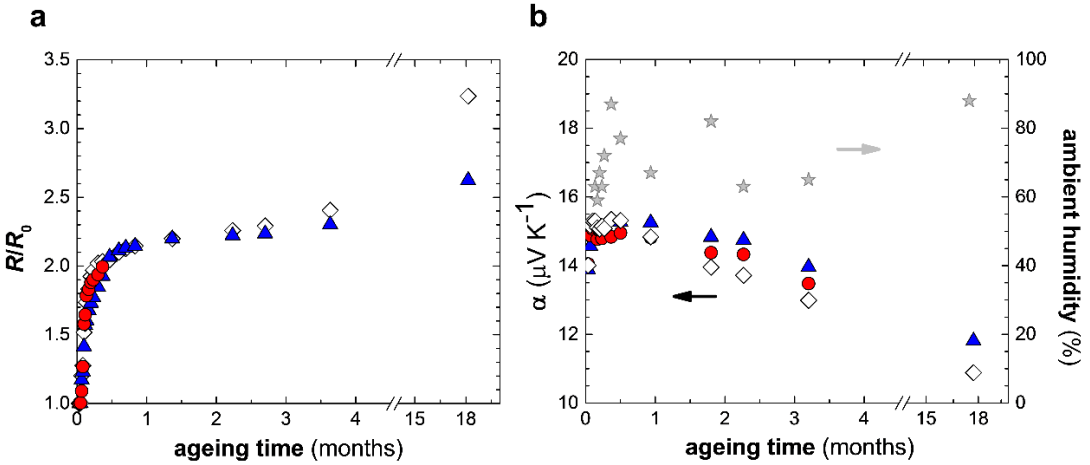

***Figure 34**. Ageing of 1 cm long segments of PEDOT:PSS dyed silk yarns under ambient conditions: (a) resistance R relative to initial resistance, R_0, (b) Seebeck coefficient, α, MeOH (◊), EG (▲), DMSO (●), and ambient humidity (stars). Reproduced with permission from the American Chemical Society.*[21]

While neutralising PEDOT:PSS was able to prevent acid hydrolysis of the cellulose in the cotton yarns, thus maintaining its mechanical strength, the dyed cotton suffered from a significant drop in conductivity c.f. non-neutralised PEDOT:PSS, with $\sigma \approx 1$ S cm^{-1} (in fact so did the silk sample with $\sigma \approx 10^{-1}$ S cm^{-1}) further highlighting the importance of electrostatic interactions. With this initial electrical and mechanical investigation, all further experiments and developments were carried out on PEDOT:PSS dyed silk systems.

Optical Imaging

Optical microscopy and scanning electron microscopy (SEM) was undertaken to analyse sample structures. A large amount of silk can be died at a time using the exhaust dyeing method (figure 35, left) and optical microscopy shows that the dyed silk takes on the colour of PEDOT:PSS (figure 35, right).

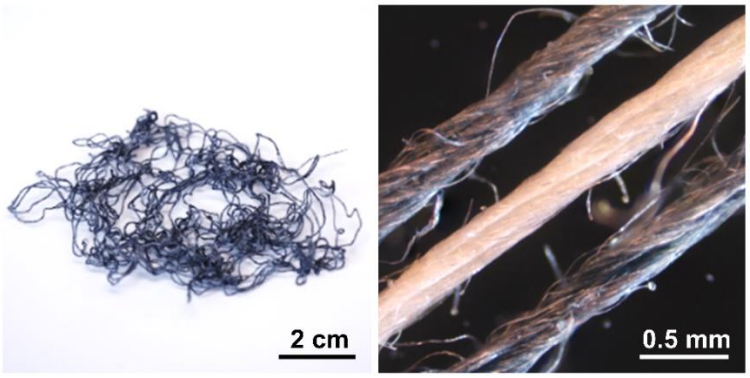

***Figure 35**. Bundle of PEDOT:PSS dyed silk yarn (left) and optical microscopy image of neat and PEDOT:PSS dyed silk yarns with a diameter $\varnothing_{yarn} \approx 0.25$ mm (right). Reproduced with permission from the American Chemical Society.*[21]

SEM analysis, undertaken by Dr Desalegn Mengistie, shows that the PEDOT:PSS is in fact dyeing the silk. By analysing non-sputtered samples (figure 36, left) the electrically insulating core and the outer layer infused with the conducting polymer can be distinguished, and impregnation of the silk is clear. Analysis of non-sputtered (figure 36, left) and sputtered (figure 36, right) samples show a certain degree of coating delamination (figure 36, arrows), which can be considered as excess coating.

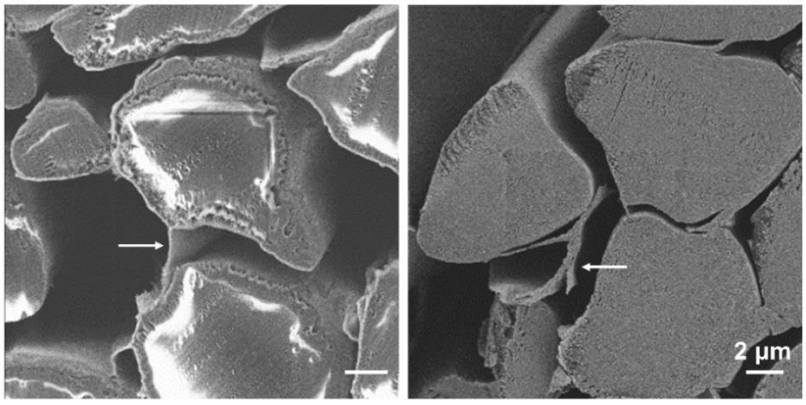

***Figure 36**. SEM images of freeze-fractured PEDOT:PSS dyed silk yarns prepared with DMSO; (right) SEM image recorded after sputtering yarns with gold. Reproduced with permission from the American Chemical Society.*[21]

Washability

Thus far, the dyed silk yarns have be characterised as having a high degree of electrical stability, mechanical robustness and flexibility. Additionally, they can be confirmed as being

machine-washable, even with commercially available washing powder. This ability for them to be machine-washed lends the conducting yarns even further to practical use in day-to-day items such as clothing, for use as "wires" or for thermoelectrics (see Chapter 6.3). Initially, it was noted that the PEDOT:PSS did not detach from the silk yarn after being submerged in water for 4 days (figure 37a), leading to washing the yarns (performed by Dr Anja Lund, Chalmers) in a commercial washing machine using 20 mL of a common washing detergent (figure 37b) on a hand wash cycle (30 ºC, 50 min, 900 rpm). Each sample was washed between 1-4 times, and after drying at room temperature for at least 6 hours (figure 37c) the electrical conductivity was measured (figure 37d), and within experimental error, no change was observed even after 4 washing cycles.

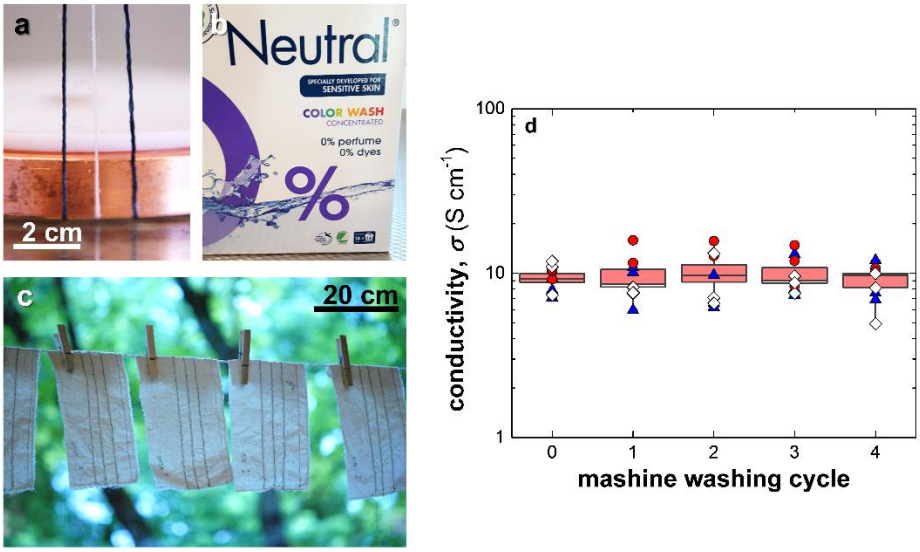

Figure 37*. (a) Neat and PEDOT:PSS dyed silk yarns submerged for 1 h in distilled water; (b) using 20 mL Neutral COLOR WASH detergent; (b) PEDOT:PSS dyed silk yarns were sewn onto cotton fabrics and washed in a household Electrolux washing machine at 30 °C for 50 min and a 900 rpm spin drying cycle; (d) electrical conductivity, σ, of PEDOT:PSS dyed silk yarns as a function of washing cycle (MeOH (◊), EG (▲), DMSO (●). Reproduced with permission from the American Chemical Society.*[21]

Dry cleaning (performed by Dr Desalegn Mengistie, Chalmers) was also investigated by submerging and gently shaking DMSO co-treated samples in the common dry cleaning solvent tetrachloroethylene for 1 hour, and after 5 consecutive washes and drying at 130 ºC for 10 min after each cycle, σ decreased by no more than a factor of 2 (see Paper III, figure S3).

6.2 n-type Yarns

In order to attain a thermoelectric module performing at its maximum potential, the previously discussed p-type yarns should be complimented with counterpart n-type yarns (see Chapter 2.2.1 – equation 11). The work undertaken in Paper IV focused upon the coating of polyethylene terephthalate (PET) yarn with the previously discussed multi-walled carbon nanotube:polyvinylpyrrolidone (MWNT:PVP) n-type system (see Chapter 5), in order to supplement the fabricated thermoelectric module system developed in Paper III (see Chapter 6.3).

6.2.1 Manufacture

First steps towards attaining an n-type fibre system focused upon the use of nitrogen doped n-type carbon nanotubes (N-MWNTs), the same 'as synthesised' nanotubes utilised in the systems of Paper II (see Chapter 5), and coating them onto silk yarn. The N-MWNTs were dispersed in water using sonication along with polystyrene sulfonate (PSS), with the intention that a similar outcome as with the previously discussed dyeing concept with PEDOT:PSS silk yarns would occur between the PSS and silk, along with the N-MWNTs bound in the PSS matrix. The N-MWNT:PSS mixture was dropped and squeezed along the silk yarn vertically, much like the methodology presented by Steven et al.[140] Unfortunately, low conductivities were attained for this system ($\sigma \approx$ 0.1 S cm^{-1}), however a suitable α of -11 µV K^{-1} was attained. Further, crosslinking the PSS with (3-glycidyloxypropyl)trimethoxysilane (GOPS), a common crosslinking agent in PEDOT:PSS systems,[141] was explored in order to aid durability and potentially introduce washability to the system. Where in fact upon post-treating the system with GOPS did allow for the coated/dyed silk yarn to be submerged without visible loss of the polymer system, no conductivity was detected, even when slightly cutting into the material to bypass outer layers.

Eventually, the nanocomposite MWNT:PVP (4:1 ratio) system presented by Sarabia-Riquelme *et al*. was utilised.[63,142] A panel of different reaction methodologies were explored in order to attain a system performing with satisfying electrical parameters (i.e. $\alpha < 0$). Applying the MWNT:PVP system directly to silk yarn proved unsuccessful with values of $\alpha \approx 2$ µV K^{-1}, the reason of which is ascribed to stronger interaction of carboxylic acid functional groups of the silk yarn with PVP, disrupting the interaction between the nanotubes and the PVP.[143,144] Attempts to shield the nanocomposite system from the silk interaction with a dilute pre-coating of PVP yielded similar results of $\alpha \approx 3$ µV K^{-1}, however, soaking the same yarn in a solution of triphenylphosphine

(TPP) (also a dopant for CNTs[60]) in acetone gave the first negative value of $\alpha \approx$ -3 µV K^{-1}. Further, pre-coating the silk with higher concentration PVP (500 g L^{-1} c.f. the previous 8 mg mL^{-1}) yielded $\alpha \approx$ -7 µV K^{-1}. Attempts to co-processes the MWNT:PVP nanocomposite with TPP in DMSO and coating to PVP pre-coated silk gave $\alpha \approx$ -3 µV K^{-1}.

With the understanding that the somewhat chemically delicate system between the MWNTs and PVP should be preserved by using non-competing substrates, further experiments focused on PET yarn as a substrate. Coating PET yarn with the concentrations provided in the work of Sarabia-Riquelme *et al*. (2 g L^{-1} MWNTs, 8 g L^{-1} PVP) was initially unsuccessful, given a lack of wetting of PET. Sarabia-Riquelme *et al*. suggest that the addition of MeOH would aid in wetting, however, this would lead to a far too dilute nanocomposite ink. Instead, PVP was added at high concentration (500 g L^{-1}) as a pre-adhesive layer. Using the relatively low concentrations reported by Sarabia-Riquelme *et al*. on pre-coated PET gave rise to α values of ≈ -5 µV K^{-1}, unfortunately still not a large enough negative Seebeck coefficient as desired. Finally, increasing the nanocomposite concentration to x5, x7.5, x10 or x15 that of the original work increased the overall negative Seebeck from ≈ -5 eventually to ≈ -14 µV K^{-1} for the most concentrated solution. Additionally, branched polyethylenimine (PEI) was added to attempt to enhance the thermoelectric properties of the material, though no significant difference between samples with or without the selected PEI quantity (0.05 wt% w.r.t. MWNT) was noted. It was observed that once dry, the PET yarn nanocomposite samples delaminated with handling and use, so in order to prevent this the block copolymer styrene-isoprene-styrene (SIS) was added to the yarns. The application of SIS did not affect the yarns, since toluene was used as a solvent which did not dissolve any of the water soluble coating. The addition of SIS to the yarns provided stability to the system whilst being handled, protection to the user to possible nanotube exposure and water resistance to the system. The experimental procedure presented in Paper IV, and the chemicals used, is summarised in figure 38.

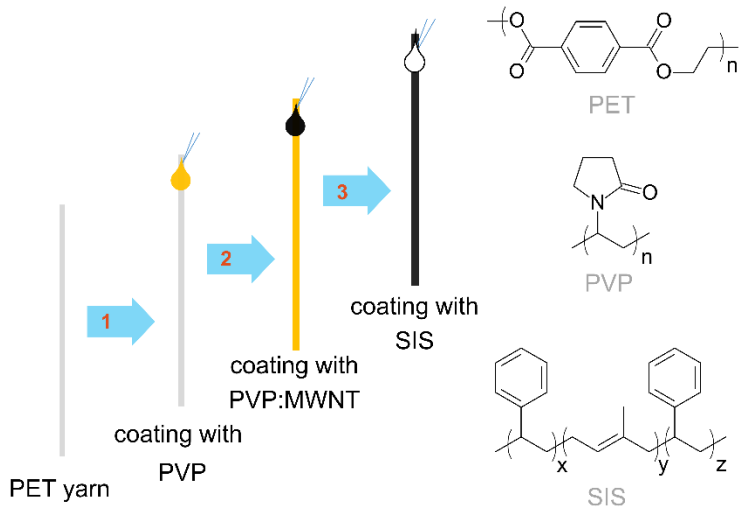

***Figure 38**. Schematic representation of the three step coating process of PET yarn with: 1) PVP adhesion layer, 2) MWNT:PVP conducting layer, and 3) outer SIS protection layer; chemical structures of PET, PVP and SIS.*[142]

6.2.2 Properties

Electrical and Mechanical

All methods used for electrical and mechanical analysis are the same as those presented in Chapter 6.1.2, '*Electrical and Mechanical'*, and all values of electrical conductivity take into account the insulating PET yarn core.

The samples presented in Paper IV were the most successful n-type yarns, based upon PET yarn pre-coated with PVP, coated with MWNT:PVP (optionally also with PEI), and post-coated with SIS (figure 38). Electrical values were found to be: $\sigma \approx 1$ S cm^{-1} and $\alpha \approx -14$ µV K^{-1}; tensile testing yielded the mechanical properties: stress at break ≈ 350 MPa, elongation at break ≈ 30 % and a Young's modulus of ≈ 3 GPa. The samples gave similar values of mechanical strength to that of neat PET yarn, further, samples with or without SIS post-coating displayed no significant difference in electrical values. Films of the MWNT:PVP(:PEI) systems were made, and showed similar values of $\alpha \approx -14$ µV K^{-1} as for the yarns. However, σ for the films were ≈ 1 S cm^{-1}. Given a weight uptake of 18% for the conducting MWNT:PVP layer, if only the nanocomposite was taken into account without the insulating PET core, a value of $\sigma \approx 5$ S cm^{-1} is attained, closer to the reported 25 S cm^{-1} for films.[63] The electrical and mechanical properties for the coated PET yarns are summarised in table 4.

			mechanical properties				electrical properties			
yarn	polymer matrix	protective coating	S_{break} (MPa)	ε_{break} (%)	E (GPa)	n	σ (S cm^{-1})	n	α (μV K^{-1})	n
PET	-	-	375 ± 18	37 ± 8	2.7 ± 0.4	3	-[a]	-	-[a]	-
	PVP	-	-[b]	-[b]	-[b]		0.8 ± 0.2	5	-12 ± 1	3
	PVP	SIS	356 ± 48	26 ± 6	3.6 ± 1.0	5	0.8 ± 0.2	5	-14 ± 1	3
	PVP:PEI	-	-[b]	-[b]	-[b]		1.0 ± 0.3	9	-14 ± 1	3
	PVP:PEI	SIS	386 ± 14	32 ± 2	2.8 ± 0.8	5	0.7 ± 0.2	5	-15 ± 1	3

Table 4. Mechanical and electrical properties of PET yarns pre-coated with PVP then coated with MWNT:PVP and finally SIS. Stress at break S_{break}, strain at break ε_{break}, Young's modulus E, electrical conductivity σ relative to the fibre cross section, and Seebeck coefficient α. All measurements were made four days after fabrication. [a]non-conducting, [b]too delicate coating for tensile drawing.[142]

Given the tendency of n-type materials to show a lack of stability due to oxidation in air, displaying the stability of the yarns presented in Paper IV is of great importance. Stability measurements of σ (figure 39a) and α (figure 39b), and also the power factor, *PF* (figure 39c), show a promising degree of ambient stability, with measurements made as long as ≈ 6 months after synthesis, highlighting the inherent stability of the system. In fact, on average, the values of σ and α increase by a factor of 2-3 over time.

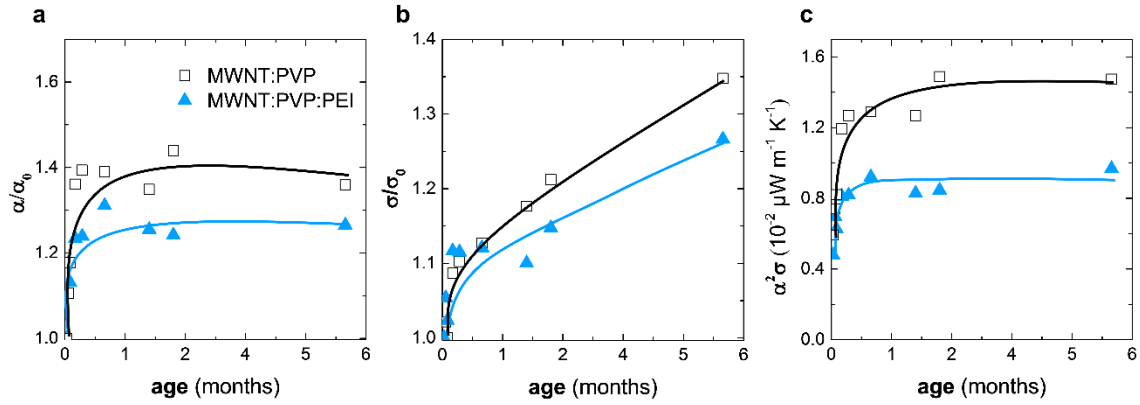

***Figure 39**. Ageing of the thermoelectric properties of MWNT:PVP coated PET yarns under ambient conditions: (a) Seebeck coefficient ($\alpha_0 \approx -11 \mu V\ K^{-1}$), (b) conductivity ($\sigma_0 \approx 0.5\ S\ cm^{-1}$), and (c) power factor $\alpha^2\sigma$ (□ MWNT:PVP, ▲ MWNT:PVP:PEI).*[142]

To further highlight the durability of the samples and to determine whether they could be used successfully in modules which require flexibility, the yarns post-coated with and without SIS were subjected to repeated bending (performed by Dr Anna Hofmann). The samples were affixed at their ends to a homemade Lego setup with PET foil as support, to ensure they bent at the same point each time (figure 40a,) (a schematic is shown in figure 40b). Values of *R* gradually increase with number of bending cycles, and after 1000 cycles both samples with and without SIS display about one order of magnitude increase (figure 40c). Thus, a small amount of bending during textile manufacture is unlikely to overly reduce the thermoelectric performance.

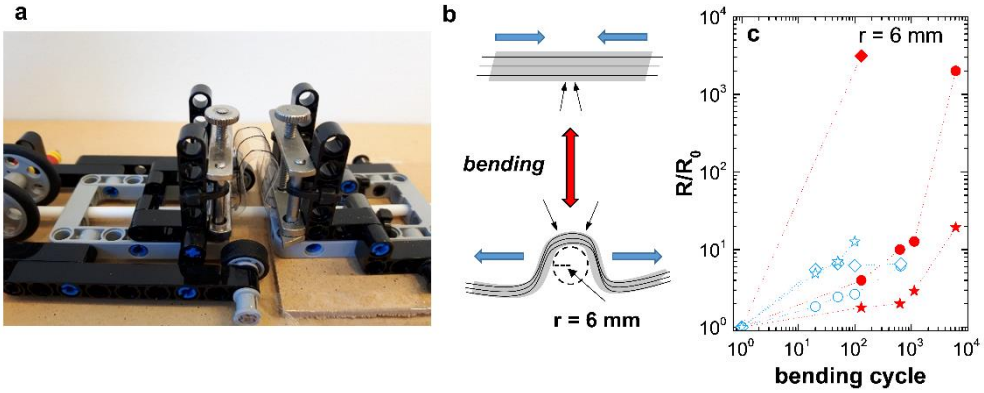

***Figure 40**. (a) Lego setup for bend testing; (b) schematic diagram of bending test performed with a Lego setup; (c) resistance R of ≈ 7 cm long yarns bent repeatedly along with a PET foil support (different symbols denote different yarn samples, filled and empty symbols represent fibres with and without SIS coating, respectively).*[142]

Optical Imaging

Optical microscopy and scanning electron microscopy (SEM) were undertaken to analyse the sample structure. Optical microscopy shows neat PET yarn (figure 41a) with a twisted smooth structure, yarn pre-coated with PVP and coated with MWNT:PVPs (figure 41b) where the topography of the PET yarn is still visible, and finally post coated with SIS to produce a smooth yarn (figure 41c); all stages of coating show that the yarn does not increase significantly in diameter. SEM analysis, undertaken by Dr Anja Lund, shows that the nanocomposite penetrates the yarn and the SIS post-coating layer does not interfere with the conducting layer (figure 41d-e).

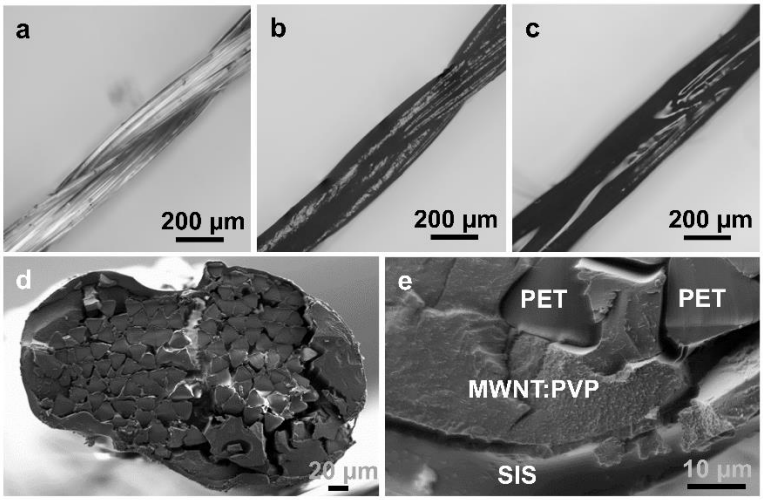

Figure 41. *Optical microscopy images of: (a) neat PET yarn, (b) PET yarn coated with PVP adhesion layer and MWNT:PVP conducting layer, (c) PET yarn coated with PVP, MWNT:PVP and SIS protection layer; (d) SEM image of the cross section of a cut PET yarn coated with PVP, MWNT:PVP and SIS protection layer, and (e) SEM image, close up of the same yarn showing the individual PET fibres embedded in the MWNT:PVP coating, surrounded by the outermost SIS coating.*[142]

Water Resistance

Supplementary to the high levels of ambient stability for the coated PET yarn system, the yarns can be also characterised as being water submersion resistant – due to the addition of SIS to the system, which is entirely non-soluble in water. The outer layer of SIS can be seen as a cable insulation with the MWNT:PVP as the conducting core. The electrical resistance was measured before, during and after submersion in water, with no notable increase in overall resistance occurring (figure 42). Concluding, the yarns are clearly suitable to be used in practical situations, including those where water contact is necessary.

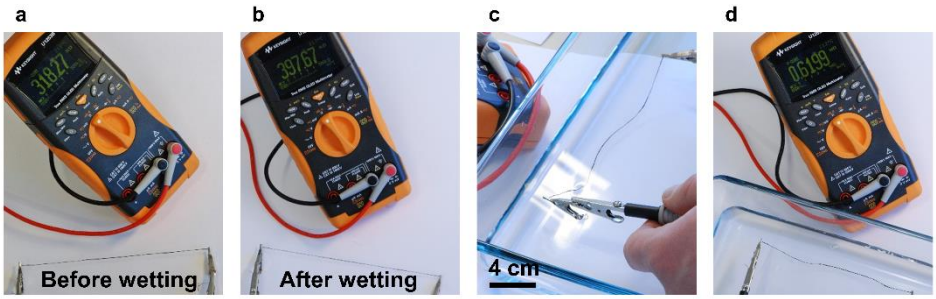

***Figure 42**. Photographs of resistance measurements of MWNT:PVP + SIS coated PET yarn before water submersion (a), during water submersion (c and d) and after submersion (b).*[142]

6.3 Thermoelectric Textile Modules

Modules: Conducting p-type Silk Yarn

In all instances, PEDOT:PSS dyed silk yarns co-treated with DMSO were used. Initially a small test device was created for the simple purpose of demonstrating the use of conducting PEDOT:PSS silk yarns as wires over a bend, when stitched onto a wool swatch. The silk was stitched with a couch stitch method between a battery and an LED, and placed around a wrist (see Paper III, figure 5a).

With confirmation that the yarns could be successfully stitched, a small test in-plane thermoelectric module was fabricated, comprised of 2 leg pairs (see Paper III, figure 5b). Each p-type leg comprised of 10 yarns of dyed silk, with a single piece of silver wire as a counterpart substitute for n-type legs. Each contact point between the legs was fixed with flexible conducting silver paste via a rubber stamp and cured at 100 ºC for 10 min; the two ends of the module was connected with silver wire in order to attach a sourcemeter. A temperature difference of up to ΔT ≈ 50 °C across the device, resulted in an open circuit voltage of $V_{oc}/\Delta T \approx 26$ µV K^{-1}, or 13 µV K^{-1} per element (solid lines Paper III, figure 5b). With the number of elements, n_e, at 2, the calculated $V_{oc}/\Delta T \approx N_{element}(\alpha_{silk} - \alpha_{silver})$ was ≈ 27 µV K^{-1} (dotted line Paper III, figure 5b), lying in close agreement with the experimentally attained value (α_{silk} = 15 µV K^{-1}, α_{silver} = 1.5 µV K^{-1}).

The cumulation of the work undertaken in Paper III resulted in the fabrication of an in-plane ‘jumbo module’ with 26 leg pairs, a scaled up and improved version of the prototype previously discussed (figure 43a). The module could be twisted repeatedly without increasing its overall internal resistance, R_{int}, of 8.7 kΩ, highlighting the inherent flexibility of the ensemble. As

with the prototype module, each p-leg possessed 10 dyed silk yarns with one silver wire counterpart, however, this time diagonally orientated to enhance efficiency of use of the space provided. The silk and silver wire were both stitched through the fabric at each leg end, and contacted with flexible curable silver paste on the back of the module (figure 43b). The module was exposed to an in-plane temperature difference of up to $\Delta T \approx 120$ °C without adverse effect on R_{int} (figure 43c), to attain an open circuit voltage of $V_{oc} \approx 37.5$ mV or $V_{oc}/\Delta T \approx 313$ µV K^{-1} (12 µV K^{-1} per element) (figure 43d). The calculated $V_{oc}/\Delta T \approx 351$ µV K^{-1} (dotted line in figure 43d) is in close agreement with the experimental value. Finally, the module was held at a $\Delta T \approx 66$ °C and connected to a series of load resistors ranging from 1 to 27 kΩ, and under load matching conditions (see Chapter 2.2.1) a maximum power output, P_{max}, of ≈ 12 nW is attained (figure 43d). With the equation $P_{max} = V_{oc}^2/4R_{int}$ the maximum power can be predicted as 12.3 nW which is in good agreement with our experimentally determined value.

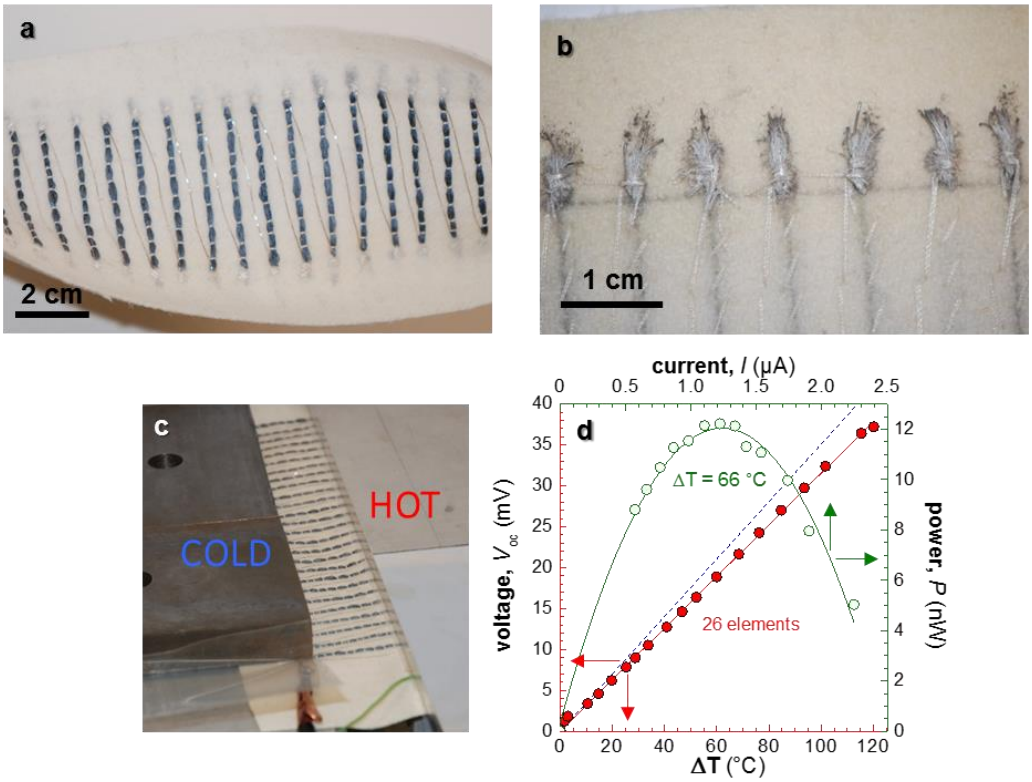

Figure 43. *(a) In-plane textile thermoelectric device with 26 p-type legs prepared in a similar way as the two leg module; (b) silver paste contacts on the backside of the felted wool fabric; (c) the device in use, suspended between a hot and cold temperature reservoir (hot plate used for hot side, steel heat sink for cold side, and PET foil as electrical insulation); (d) electrical measurements of the 26 leg module, showing V_{out} as a function of ΔT (all elements (red line), calculated (dotted line) $V_{oc}/\Delta T$; see (see Paper III, figure 5b for comparison) and power output $P = V_{oc}I$ as a function of measured current I for $\Delta T \approx 66$ °C using load resistors ranging from $R_{load} = 1$ to 27 kΩ. Reproduced with permission from the American Chemical Society.*[21]

Modules: Conducting n-type PET & p-type Silk Yarns Combined

Much like the work in Paper III, the work of Paper IV cumulated in the creation of thermoelectric modules. For p-type legs the PEDOT:PSS DMSO co-treated silk yarn system of Paper III was used (see Chapter 6.1) and for n-type legs the MWNT:PVP PET yarn system was used (see Chapter 6.2). The specific batch of p-type yarns fabricated for both the following modules possessed the thermoelectric properties: $\sigma \approx 15$ S cm^{-1} and $\alpha_{silk} \approx 15$ μV K^{-1}; the p-type yarn α is a similar absolute but positive value as for the n-type PET yarns (PET yarns $\alpha_{PET} \approx -14$ μV K^{-1}), however the p-type yarn σ is one order of magnitude higher than the n-type PET yarns (PET yarns $\sigma \approx 1$ S cm^{-1}).

Initially, a prototype module was created in order to explore the suitability of the n-type yarns for thermoelectric textile applications. The in-plane module comprised 4 elements, with 2 p-type yarns and 11 n-type yarns per element, 7 cm long each, attached using couch stitches (see Paper IV, figure 6a). Each n-type yarn was coated with SIS for the middle 5 cm, leaving 1 cm either end for electrical contact. Electrical contacts were made with flexible silver paste, cured at 100 ºC for 10 min and connections at the ends of the module were made with silver wire. At this point, electrical resistance matching between the legs to lower R_{int} (thus maximising possible power output, see Chapter 2.2.1) was a secondary concern, as this was not the main focus towards the development of a prototype module. The module consisted of 2 p-type and 11 n-type yarns per element; the total R_{int} of the module ≈ 34 kΩ. The device was then exposed to an in-plane $\Delta T \approx$ 80 ºC, to which the device attained $V_{oc} \approx 8$ mV, or $V_{oc}/\Delta T \approx 104$ µV K^{-1} (see Paper IV, figure 6b). The calculated $V_{oc}/\Delta T \approx N_{element}(\alpha_{silk} - \alpha_{PET})$ was determined as ≈ 116 µV K^{-1}, which is in close agreement to the experimental value (see Paper IV, figure 6b, dotted line). Further, P_{max} was determined for the module at $\Delta T \approx$ 80 °C by connecting to a series of load currents, to give an experimentally determined $P_{max} \approx 0.65$ nW (see Paper IV, figure 6b). A calculated $P_{max} = V_{oc}^2/4R_{int}$ is predicted to be 0.49 nW, within a reasonable margin to the experimentally determined value.

Finally, a fully functioning, *all-organic* thermoelectric textile 'mega module' was fabricated and tested (figure 44). This module improved upon the 'jumbo module' of Paper III, by including more thermoelectric elements (38 c.f. 26), and by incorporating n-type PET yarns as counter parts (as featured in Paper IV prototype module). Further, optimisation of yarn quantity per element area was considered; calculated as per Chapter 2.2.1, where the ratio of legs per set area for maximum power generation can be described as $\sqrt{\sigma_p/\sigma_n} = \sqrt{14/1} \approx 4$. In this module 3 n-type yarns were used per n-leg and one p-type yarn per p-leg (each leg 4 cm long), in near match to the 1:4 ratio calculated (the amount of available materials limited n-type yarn production). As with the prototype module, the n-type yarns were coated with SIS, however, in this case all the yarn was coated and the ends cut in order to reveal the conducting core. Electrical contacts were made with flexible carbon black paste dried at 80 ºC for 12 min then cured at 140 ºC for 2 min; connections were made at the module ends with conducting silk yarn with a little carbon black paste to improve electrical contact.

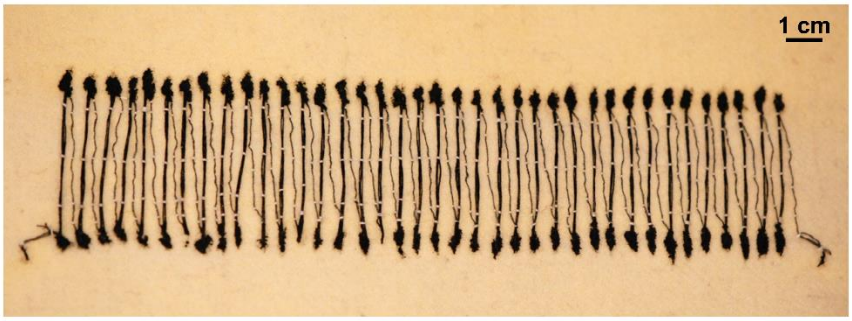

***Figure 44**. All-organic in-plane textile thermoelectric device with 38 elements, constructed with n-type coated PET yarns (3 yarns per leg), p-type silk yarns (1 yarn per leg) and a conducting carbon-based paste for electrical connections.*[142]

The module was held at an in-plane temperature difference of $\Delta T \approx 116$ ºC (figure 45a) to attain $V_{oc} \approx 143$ mV, or $V_{oc}/\Delta T \approx 1.23$ mV K^{-1} which corresponds to ≈ 23 µV K^{-1} per element (figure 45b). The experimentally determined value is slightly higher than the calculated $V_{oc}/\Delta T \approx 1.10$ mV K^{-1} (figure 45b, dotted line). Also, P_{max} was determined from connection to a series of load currents at $\Delta T \approx 80$ °C, with $R_{int} \approx 334$ kΩ for the module, to yield $P_{max} \approx 7.1$ nW (figure 45b), which is in close agreement to the calculated $P_{max} \approx 7.4$ nW.

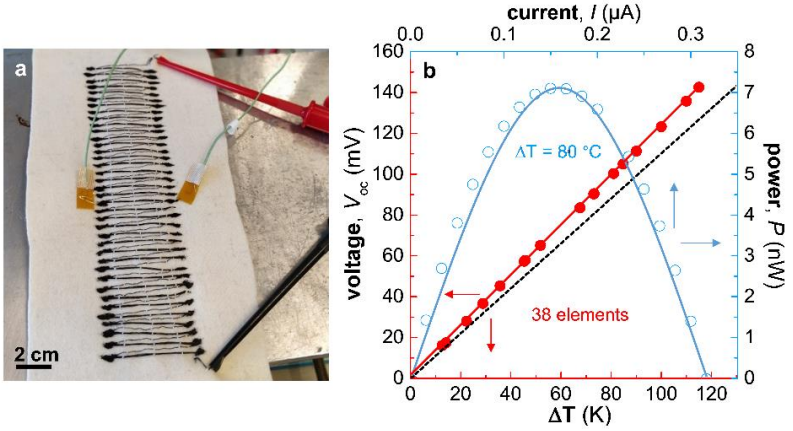

***Figure 45**. (a) All-organic in-plane embroidered textile thermoelectric device suspended between a hot and cold plate, with two adhesive thermocouples on top; (b) electrical measurements of the module with measured output voltage V_{out} as a function of ΔT (red line), as well as power output $P = V_{out}I$ as a function of measured current I for $\Delta T \approx 80$ ℃, calculated according to Chapter 2 equation 11.*[142]

Lastly, thermal imaging was used to analyse the thermal gradient lying parallel to the legs of the 'mega module' (figure 46a). When assuming a thermal emissivity of 0.95, the temperature

gradient shape over the module could be determined (figure 46b). It is concluded that with increasing distance from the hot plate heat source the temperature first decreases by ≈ 3 ºC mm^{-1} followed by ≈ 1 ºC mm^{-1} after 10 mm, which then reaches a near constant temperature at the steel cold sink edge. From this it can be concluded that the material that experiences a temperature gradient is about 2.5 to 3 cm long, thus reducing the current leg length of 4 cm could allow for greater maximum power by reducing the resistance of the legs.

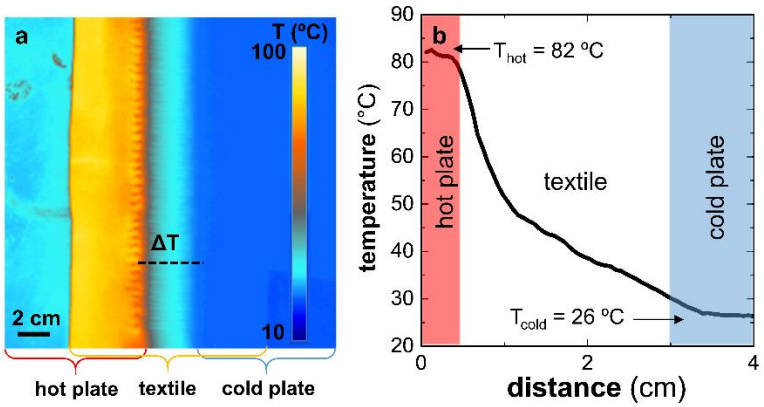

***Figure 46**. (a) Thermal image of the module, placed as in (Figure 45a), with T_{hot} ≈ 82 ºC and T_{cold} ≈ 26 ºC (note that in the image the bare hot plate appears to be cold, due to the relatively low emissivity of aluminium); (b) temperature gradient across the textile device (see dashed line in a), T_{hot} and T_{cold} measured with thermocouples (red box = hot plate; blue box = cold plate).*[142]

Chapter 7

CONCLUDING REMARKS AND OUTLOOK

In conclusion, we have taken steps towards enhancing the understanding of thermoelectric systems, added to the current library of bulk materials that are available for thermoelectrics, and created devices to demonstrate new and exciting possibilities towards thermoelectric energy harvesting with relatively simple and robust methodologies.

We have developed highly durable conductive silk yarns via dyeing with PEDOT:PSS. The yarns, produced via exhaust dying, could be made in the 10s of meters. They show a wide variety of properties including high tensile modulus (~ 2 GPa) as well as durability and resilience towards 'wear and tear' during bending and sewing. These yarns proved to be machine washable without loss of conductivity, and to further prove their usefulness and applicability, a 'jumbo' module was created with 26 elements providing $V_{oc}/\Delta T \approx 0.31$ mV K^{-1} and $P_{max} \approx 12$ nW.

Complementing the work undertaken with p-type yarns, we have also developed conductive n-type PET yarns (via coating with an organic nanocomposite) which show long term stability under ambient conditions. The yarns demonstrated resistance to water and some bending (when further coated with the polymer SIS), which could prove useful for mechanical stitching. Finally, an *all-organic* thermoelectric 'mega' module was fabricated with 38 elements, utilising the previously fabricated silk yarns as p-legs, which provided $V_{oc}/\Delta T \approx 1.23$ mV K^{-1} and $P_{max} \approx 7$ nW.

We demonstrated carbon nanotube composites which show either positive or negative Seebeck coefficients by simply tuning the composite concentrations. Additionally, UV photoswitching of a single carbon nanotube composite 'ink' leads to a switch from p- to n-type; particularly of interest to large area coasting and printing processes, by reducing complexity to simple patterning. Further, the applicability of millimetre-thick materials for thermoelectrics was enhanced with the development of a foamed P3HT polymeric material which allows for doping its thick structure. Additionally, the foamed material does not significantly suffer from the foaming process.

This thesis has displayed in-plane thermoelectric devices, with focus on material properties. Logically the next step would be to develop out-of-plane devices to enable a vastly larger amount of thermoelectric elements to be present in a module. This goal can be facilitated by upscaling material production and incorporating industrial methodologies for generating large, high density (in terms of element spacing and effective element area) thermoelectric generators. Optimisation of the geometries of the modules should also be considered, with the length and area of the legs, to attain a greater power output.

Further, the materials can be improved by diverting attention away from dying and coating, and instead developing bulk fibres. In this way a material would not suffer from a large insulating core which overall does not contribute to the thermoelectric properties. However, bulk fibres would need to attain mechanical robustness from the active material, which could be improved with additive polymers, for example with polyurethane, assuming they are compatible with the active system.

ACKNOWLEDGEMENTS

So, here we are at the end, in more ways than one. However, if you're the average PhD student, welcome, as this is usually the first thing we read in a thesis. Here we go, so don't cry guys!

My time as a student living in Sweden has certainly had its up's and down's, but thanks to some great people both past and present, I can certainly say the up's have the win.

My particular special thanks go to Christian '*the boss*' Müller for help and guidance and most of all being a present supervisor who always has time for his students.

The Crew, you are all so important to me, so alphabetical it is: Ali, Ambra, AnnaP, AnnaR, Fanny, Ida! Thank you for making complete the social side of my stay in Sweden. Our adventures were numerous, and hopefully not at an end!

Amaia, Chickitaa, of course you get your own shout-out. My academic partner-in-crime and best friend, thanks for all, always being there for me and always accepting me for me.

My group colleagues and friends, the dream-team!: Mattias, David, Jonna, AnnaP, Liyang, Renee, Anja, Ida, AnnaH, Khalid, Yingwei, Sozan, Sandra, Sepideh, Emmy, Dominik, you guys are awesome and great to work with. Massi, special thanks for your friendship, support and being my climbing buddy! Stepan, my oldest friend, I hope we get to live on the same continent soon to take up again some of the good ol' craft beer and shisha fun.

Mariano Campoy-Quiles and Bernhard Dörling of ICMAB, for hosting me as a visiting PhD student, thank you for a great stay, and getting me started with the first paper of my PhD.

Alicja, the one I annoy the most but supports me in equal measure, thank you for your help, support and your care. I look forward very much to the next adventures!

Lotta and Frida, the champions of the division, keeping everything moving and working like a well-oiled machine.

Anders Palmqvist my co-supervisor, examiner and division head, thank you for your care and always making time for me when I needed it.

My mom: there is not much to say that we don't already know, but in brief, thanks for always being there for me and supporting and always been proud of me no matter what!

Brendan, keep up the good work, never give up and make it all the way. Thanks for all the wrestling matches (which I still win ;)), maybe one day dear bro haha.

Finally, a message to my fellow PhD students in fact anyone on a difficult journey, remember a quote from a wise hero: "Why do we fall? So that we can learn to pick ourselves back up." – Bruce Wayne/Batman

Jason

APPENDIX - CHEMICAL STRUCTURES

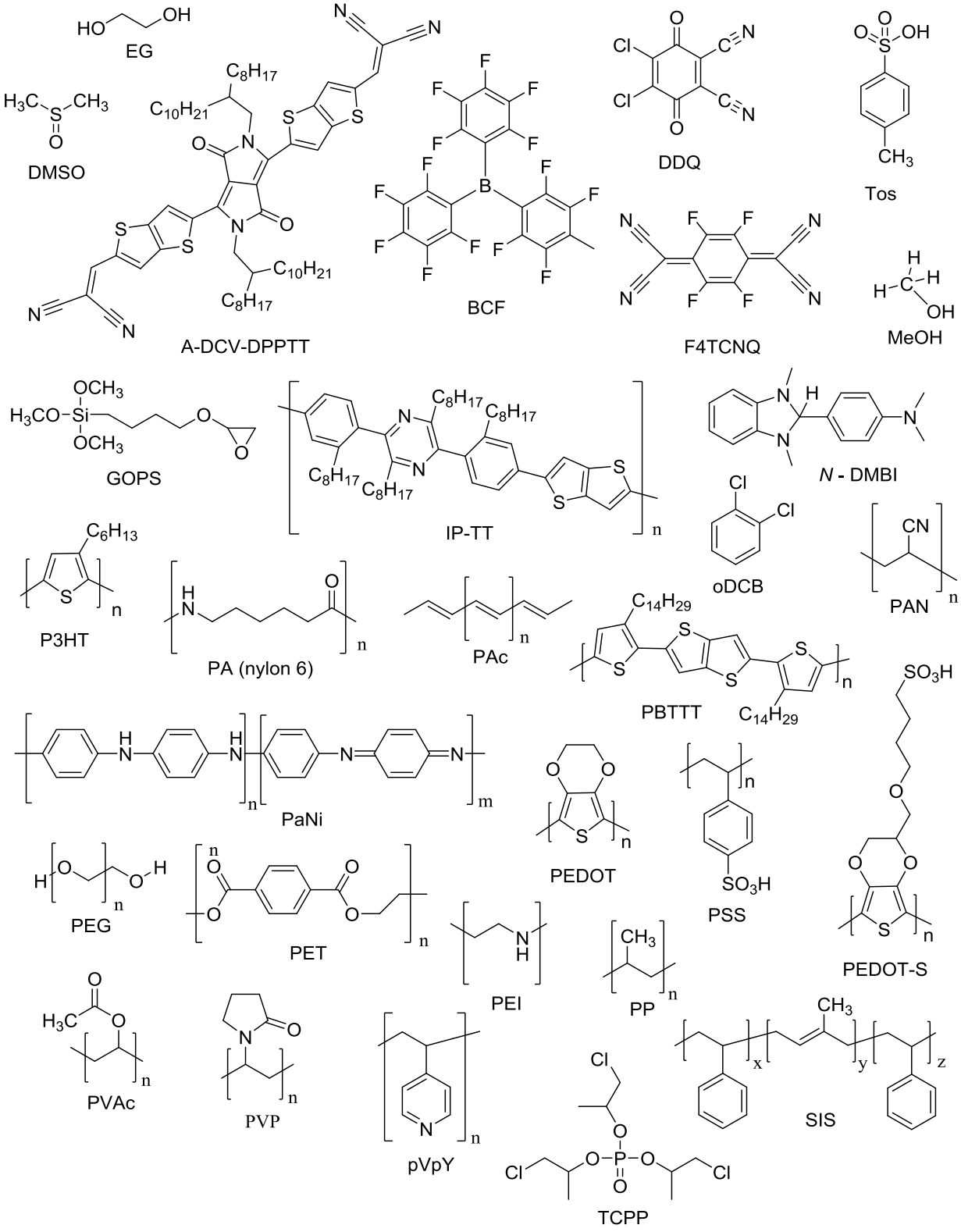

BIBLIOGRAPHY

1. R. R. Sondergaard, M. Hosel, N. Espinosa, M. Jorgensen and F. C. Krebs, *Energy Sci Eng*, 2013, **1**, 81-88.
2. H. J. Findley, *US Pat.*, 2519241, 1950.
3. B. Nishanth, D. S. Kumar, A. Naveen, R. Vijayanandh and M. S. Kumar, *Mater Today-Proc*, 2017, **4**, 8378-8386.
4. P. Tatry and S. Berhouet, *US Pat.*, 14694638, 2015.
5. D. J. Bents, *NASA Technical Memorandum*, Report 102003, NASA, US, 1989.
6. NASA, Mars 2020 Rover, mars.nasa.gov/mars2020
7. R. Kroon, D. A. Mengistie, D. Kiefer, J. Hynynen, J. D. Ryan, L. Y. Yu and C. Muller, *Chem Soc Rev*, 2016, **45**, 6147-6164.
8. S. van Reenen and M. Kemerink, *Org Electron*, 2014, **15**, 2250-2255.
9. A. M. Glaudell, J. E. Cochran, S. N. Patel and M. L. Chabinyc, *Adv Energy Mater*, 2015, **5**.
10. G. Z. Zuo, Z. J. Li, E. G. Wang and M. Kemerink, *Adv Electron Mater*, 2018, **4**.
11. T. Bashir, L. Fast, M. Skrifvars and N. K. Persson, *J Appl Polym Sci*, 2012, **124**, 2954-2961.
12. I. Miccoli, F. Edler, H. Pfnur and C. Tegenkamp, *J Phys-Condens Mat*, 2015, **27**.
13. L. J. van der Pauw, *Philips Res Rep*, 1958, **13**, 1-9.
14. J. Liu, X. J. Wang, D. Y. Li, N. E. Coates, R. A. Segalman and D. G. Cahill, *Macromolecules*, 2015, **48**, 585-591.
15. P. Krupa and S. Malinaric, *Int J Mech and Mech Eng*, 2014, **8**, 735-740.
16. HotDiskInstruments, Technology, hotdiskinstruments.com/technology
17. C. Dixon, M. R. Strong and S. M. Zhang, *P Soc Photo-Opt Ins*, 2000, **4339**, 362-370.
18. O. M. Corbino, *Atti della Reale Accade mia Nazionale die Lincei*, 1912, **21**, 181-188.
19. D. Z. Huang, H. Y. Yao, Y. T. Cui, Y. Zou, F. J. Zhang, C. Wang, H. G. Shen, W. L. Jin, J. Zhu, Y. Diao, W. Xu, C. A. Di and D. B. Zhu, *J Am Chem Soc*, 2017, **139**, 13013-13023.
20. Y. Du, K. F. Cai, S. Chen, H. X. Wang, S. Z. Shen, R. Donelson and T. Lin, *Sci Rep-Uk*, 2015, **5**.
21. J. D. Ryan, D. A. Mengistie, R. Gabrielsson, A. Lund and C. Muller, *Acs Appl Mater Inter*, 2017, **9**, 9045-9050.
22. P. Li, Y. Guo, J. K. Mu, H. Z. Wang, Q. H. Zhang and Y. G. Li, *Rsc Adv*, 2016, **6**, 90347-90353.
23. K. Kirihara, Q. Wei, M. Mukaida and T. Ishida, *Synthetic Met*, 2017, **225**, 41-48.
24. R. He, G. Schierning and K. Nielsch, *Adv Mater Technol-Us*, 2018, **3**.
25. T. L. Sun, J. L. Peavey, M. D. Shelby, S. Ferguson and B. T. O'Connor, *Energ Convers Manage*, 2015, **103**, 674-680.
26. G. Min and D. M. Rowe, *Semicond Sci Tech*, 2007, **22**, 880-883.

27. J. Weber, K. Potje-Kamloth, F. Haase, P. Detemple, F. Voklein and T. Doll, *Sensor Actuat a-Phys*, 2006, **132**, 325-330.
28. A. Fabian-Mijarigos, G. Min and J. Alvarez-Quintana, *Energ Convers Manage*, 2017, **148**, 1372-1381.
29. A. Lund, N. v. d. Velden, N. K. Persson, M. Hamedi and C. Müller, *Mater Sci Eng R: Rep*, 2018, **126**, 1-29.
30. C. Yi, A. Wilhite, L. Zhang, R. D. Hu, S. S. C. Chuang, J. Zheng and X. Gong, *Acs Appl Mater Inter*, 2015, **7**, 8984-8989.
31. S. N. Patel, A. M. Glaudell, K. A. Peterson, E. M. Thomas, K. A. O'Hara, E. Lim and M. L. Chabinyc, *Sci Adv*, 2017, **3**.
32. R. Kroon, J. D. Ryan, D. Kiefer, L. Y. Yu, J. Hynynen, E. Olsson and C. Muller, *Adv Funct Mater*, 2017, **27**.
33. Y. Liu, J. K. Boyles, J. Genzer and M. D. Dickey, *Soft Matter*, 2012, **8**, 1764-1769.
34. T. G. Leong, B. R. Benson, E. K. Call and D. H. Gracias, *Small*, 2008, **4**, 1605-1609.
35. X. Y. Guo, H. Li, B. Y. Ahn, E. B. Duoss, K. J. Hsia, J. A. Lewis and R. G. Nuzzo, *P Natl Acad Sci USA*, 2009, **106**, 20149-20154.
36. L. Ionov, *Soft Matter*, 2011, **7**, 6786-6791.
37. C. K. Chiang, C. R. Fincher, Y. W. Park, A. J. Heeger, H. Shirakawa, E. J. Louis, S. C. Gau and A. G. Macdiarmid, *Phys Rev Lett*, 1977, **39**, 1098-1101.
38. H. Y. Yao, Z. Fan, H. L. Cheng, X. Guan, C. Wang, K. Sun and J. Y. Ouyang, *Macromol Rapid Comm*, 2018, **39**.
39. R. Kroon, M. Lenes, J. C. Hummelen, P. W. M. Blom and B. De Boer, *Polym Rev*, 2008, **48**, 531-582.
40. C. Liu, K. Wang, X. Gong and A. J. Heeger, *Chem Soc Rev*, 2016, **45**, 4825-4846.
41. D. Gedefaw, M. Prosa, M. Bolognesi, M. Seri and M. R. Andersson, *Adv Energy Mater*, 2017, **7**.
42. M. Hess, R. G. Jones, J. Kahovec, T. Kitayama, P. Kratochvil, P. Kubisa, W. Mormann, R. F. T. Stepto, D. Tabak, J. Vohlidal and E. S. Wilks, *Pure Appl Chem*, 2006, **78**, 2067-2074.
43. K. Shi, F. J. Zhang, C. A. Di, T. W. Yan, Y. Zou, X. Zhou, D. B. Zhu, J. Y. Wang and J. Pei, *J Am Chem Soc*, 2015, **137**, 6979-6982.
44. H. Mendez, G. Heimel, A. Opitz, K. Sauer, P. Barkowski, M. Oehzelt, J. Soeda, T. Okamoto, J. Takeya, J. B. Arlin, J. Y. Balandier, Y. Geerts, N. Koch and I. Salzmann, *Angew Chem Int Edit*, 2013, **52**, 7751-7755.
45. I. Salzmann, G. Heimel, M. Oehzelt, S. Winkler and N. Koch, *Accounts Chem Res*, 2016, **49**, 370-378.
46. S. Ukai, H. Ito, K. Marumoto and S. I. Kuroda, *J Phys Soc Jpn*, 2005, **74**, 3314-3319.
47. H. C. F. Martens, I. N. Hulea, I. Romijn, H. B. Brom, W. F. Pasveer and M. A. J. Michels, *Phys Rev B*, 2003, **67**.
48. P. Pingel, M. Arvind, L. Kolln, R. Steyrleuthner, F. Kraffert, J. Behrends, S. Janietz and D. Neher, *Adv Electron Mater*, 2016, **2**.

49. Y. Han, G. Barnes, Y. H. Lin, J. Martin, M. Al-Hashimi, S. Y. AlQaradawi, T. D. Anthopoulos and M. Heeney, *Chem Mater*, 2016, **28**, 8016-8024.
50. S. S. Pandey, W. Takashima, S. Nagamatsu, T. Endo, M. Rikukawa and K. Kaneto, *Jpn J Appl Phys 2*, 2000, **39**, L94-L97.
51. J. Hynynen, D. Kiefer and C. Muller, *Rsc Adv*, 2018, **8**, 1593-1599.
52. P. Pingel and D. Neher, *Phys Rev B*, 2013, **87**.
53. J. Hynynen, D. Kiefer, L. Y. Yu, R. Kroon, R. Munir, A. Amassian, M. Kemerink and C. Muller, *Macromolecules*, 2017, **50**, 8140-8148.
54. D. Kiefer, L. Y. Yu, E. Fransson, A. Gomez, D. Primetzhofer, A. Amassian, M. Campoy-Quiles and C. Muller, *Adv Sci*, 2017, **4**.
55. I. E. Jacobs, E. W. Aasen, J. L. Oliveira, T. N. Fonseca, J. D. Roehling, J. Li, G. W. Zhang, M. P. Augustine, M. Mascal and A. J. Moule, *J Mater Chem C*, 2016, **4**, 3454-3466.
56. A. I. Hofmann, E. Cloutet and G. Hadziioannou, *Adv Electron Mater*, 2018, **0**, 1700412.
57. A. Elscher, S. Kirchmeyer, W. Lövenich, U. Merker and K. Reuter, *PEDOT: Principles and Applications of an Intrinsically Conductive Polymer*, CRC Press, Boca Raton, 2011, 377
58. J. L. Blackburn, A. J. Ferguson, C. Cho and J. C. Grunlan, *Adv Mater*, 2018, **30**.
59. D. Khim, K. J. Baeg, M. Caironi, C. Liu, Y. Xu, D. Y. Kim and Y. Y. Noh, *Adv Funct Mater*, 2014, **24**, 6252-6261.
60. Y. Nonoguchi, K. Ohashi, R. Kanazawa, K. Ashiba, K. Hata, T. Nakagawa, C. Adachi, T. Tanase and T. Kawai, *Sci Rep-Uk*, 2013, **3**.
61. R. Andrews, D. Jacques, D. L. Qian and T. Rantell, *Accounts Chem Res*, 2002, **35**, 1008-1017.
62. B. Dorling, J. D. Ryan, J. D. Craddock, A. Sorrentino, A. El Basaty, A. Gomez, M. Garriga, E. Pereiro, J. E. Anthony, M. C. Weisenberger, A. R. Goni, C. Muller and M. Campoy-Quiles, *Adv Mater*, 2016, **28**, 2782-2789.
63. R. Sarabia-Riquelme, J. Craddock, E. A. Morris, D. Eaton, R. Andrews, J. Anthony and M. C. Weisenberger, *Synthetic Met*, 2017, **225**, 86-92.
64. N. C. Hilyard and A. Cunningham, *Low density cellular plastics - Physical basis of behaviour*, Chapman and Hall, London, 1994,
65. J. Gagliani and D. E. Supkis, *Acta Astronaut*, 1980, **7**, 653-683.
66. C. Forest, P. Chaumont, P. Cassagnau, B. Swoboda and P. Sonntag, *Prog Polym Sci*, 2015, **41**, 122-145.
67. A. Berg and Z. Eckmayer, *US Pat.*, 4320201, 1982.
68. K. Kang, S. Watanabe, K. Broch, A. Sepe, A. Brown, I. Nasrallah, M. Nikolka, Z. P. Fei, M. Heeney, D. Matsumoto, K. Marumoto, H. Tanaka, S. Kuroda and H. Sirringhaus, *Nat Mater*, 2016, **15**, 896-+.
69. D. T. Scholes, S. A. Hawks, P. Y. Yee, H. Wu, J. R. Lindemuth, S. H. Tolbert and B. J. Schwartz, *J Phys Chem Lett*, 2015, **6**, 4786-4793.

70. D. T. Duong, C. C. Wang, E. Antono, M. F. Toney and A. Salleo, *Org Electron*, 2013, **14**, 1330-1336.
71. J. Li, C. W. Rochester, I. E. Jacobs, E. W. Aasen, S. Friedrich, P. Stroeve and A. J. Moule, *Org Electron*, 2016, **33**, 23-31.
72. A. T. Kleinschmidt, S. E. Root and D. J. Lipomi, *J Mater Chem A*, 2017, **5**, 11396-11400.
73. J. Li, C. Koshnick, S. O. Diallo, S. Ackling, D. M. Huang, I. E. Jacobs, T. F. Harrelson, K. Hong, G. Zhang, J. Beckett, M. Mascal and A. J. Moule, *Macromolecules*, 2017, **50**, 5476-5489.
74. Y. Y. Hsu, J. D. Gresser, D. J. Trantolo, C. M. Lyons, P. R. J. Gangadharam and D. L. Wise, *J Biomed Mater Res*, 1997, **35**, 107-116.
75. Y. S. Nam, J. J. Yoon and T. G. Park, *J Biomed Mater Res*, 2000, **53**, 1-7.
76. R. G. J. C. Heijkants, R. V. Van Calck, J. H. De Groot, A. J. Pennings and A. J. Schouten, *J Polym Sci Pol Phys*, 2005, **43**, 716-723.
77. R. G. J. C. Heijkants, R. V. van Calck, T. G. van Tienen, J. H. de Groot, A. J. Pennings, P. Buma, R. P. H. Veth and A. J. Schouten, *J Biomed Mater Res A*, 2008, **87a**, 921-932.
78. M. P. Gordon, E. W. Zaia, P. Zhou, B. Russ, N. E. Coates, A. Sahu and J. J. Urban, *J Appl Polym Sci*, 2017, **134**.
79. F. G. Cuevas, J. M. Montes, J. Cintas and P. Urban, *J Porous Mat*, 2009, **16**, 675-681.
80. M. Abderrahmene, B. AbdelIllah and G. Fouad, *Enrgy Proced*, 2017, **139**, 718-724.
81. A. Kim, M. A. Hasan, S. H. Nahm and S. S. Cho, *Compos Struct*, 2005, **71**, 191-198.
82. R. Goodall, L. Weber and A. Mortensen, *J Appl Phys*, 2006, **100**.
83. A. Schinwald, F. A. Murphy, A. Prina-Mello, C. A. Poland, F. Byrne, D. Movia, J. R. Glass, J. C. Dickerson, D. A. Schultz, C. E. Jeffree, W. MacNee and K. Donaldson, *Toxicol Sci*, 2012, **128**, 461-470.
84. H. Maruyama, R. Kariya and F. Arai, *Appl Phys Lett*, 2013, **103**.
85. A. E. Aliev, M. H. Lima, E. M. Silverman and R. H. Baughman, *Nanotechnology*, 2010, **21**.
86. A. Duzynska, A. Taube, K. P. Korona, J. Judek and M. Zdrojek, *Appl Phys Lett*, 2015, **106**.
87. Z. D. Han and A. Fina, *Prog Polym Sci*, 2011, **36**, 914-944.
88. T. K. Gupta and S. Kumar, *4- Fabrication of Carbon Nanotube/Polymer Nanocomposites*, Elsevier, The Netherlands, 2018, 61-81
89. J. H. Hsu, W. Choi, G. Yang and C. Yu, *Org Electron*, 2017, **45**, 182-189.
90. E. J. Bae, Y. H. Kang, K. S. Jang and S. Y. Cho, *Sci Rep-Uk*, 2016, **6**.
91. W. Lee, Y. H. Kang, J. Y. Lee, K. S. Jang and S. Y. Cho, *Rsc Adv*, 2016, **6**, 53339-53344.
92. C. Cho, K. L. Wallace, P. Tzeng, J. H. Hsu, C. Yu and J. C. Grunlan, *Adv Energy Mater*, 2016, **6**.

93. C. J. An, Y. H. Kang, A. Y. Lee, K. S. Jang, Y. Jeong and S. Y. Cho, *Acs Appl Mater Inter*, 2016, **8**, 22142-22150.
94. C. T. Hong, W. Lee, Y. H. Kang, Y. Yoo, J. Ryu, S. Y. Cho and K. S. Jang, *J Mater Chem A*, 2015, **3**, 12314-12319.
95. G. P. Moriarty, K. Briggs, B. Stevens, C. Yu and J. C. Grunlan, *Energy Technol-Ger*, 2013, **1**, 265-272.
96. G. P. Moriarty, S. De, P. J. King, U. Khan, M. Via, J. A. King, J. N. Coleman and J. C. Grunlan, *J Polym Sci Pol Phys*, 2013, **51**, 119-123.
97. N. E. Coates, S. K. Yee, B. McCulloch, K. C. See, A. Majumdar, R. A. Segalman and J. J. Urban, *Adv Mater*, 2013, **25**, 1629-1633.
98. C. Yu, K. Choi, L. Yin and J. C. Grunlan, *Acs Nano*, 2011, **5**, 7885-7892.
99. C. Z. Meng, C. H. Liu and S. S. Fan, *Adv Mater*, 2010, **22**, 535-+.
100. K. C. See, J. P. Feser, C. E. Chen, A. Majumdar, J. J. Urban and R. A. Segalman, *Nano Lett*, 2010, **10**, 4664-4667.
101. J. J. Luo, G. Cerretti, B. Krause, L. Zhang, T. Otto, W. Jenschke, M. Ullrich, W. Tremel, B. Voit and P. Potschke, *Polymer*, 2017, **108**, 513-520.
102. S. L. Kim, K. Choi, A. Tazebay and C. Yu, *Acs Nano*, 2014, **8**, 2377-2386.
103. C. H. Yu, A. Murali, K. W. Choi and Y. Ryu, *Energ Environ Sci*, 2012, **5**, 9481-9486.
104. D. Qian, R. Andrews, M. Weisenberger and M. S. Meier, *Nanomaterials and Energy*, 2012, **1**, 168-179.
105. D. Jacques and R. Andrews, *US Pat.*, 7504078B1, 2007.
106. D. jacques and R. Andrews, *US Pat.*, 7160531B1, 2009.
107. S. D. Stranks, C. Weisspfennig, P. Parkinson, M. B. Johnston, L. M. Herz and R. J. Nicholas, *Nano Lett*, 2011, **11**, 66-72.
108. G. J. Hu, C. G. Zhao, S. M. Zhang, M. S. Yang and Z. G. Wang, *Polymer*, 2006, **47**, 480-488.
109. F. F. Lian, J. P. Llinas, Z. Y. Li, D. Estrada and E. Pop, *Appl Phys Lett*, 2016, **108**.
110. H. Wang, J. H. Hsu, S. I. Yi, S. L. Kim, K. Choi, G. Yang and C. Yu, *Adv Mater*, 2015, **27**, 6855-+.
111. D. Nassyrov, C. Muller, A. Roige, I. Burgues-Ceballos, J. O. Osso, D. B. Amabilino, M. Garriga, M. I. Alonso, A. R. Goni and M. Campoy-Quiles, *J Mater Chem*, 2012, **22**, 4519-4526.
112. S. H. Wang, H. D. Sun, U. Ail, M. Vagin, P. O. A. Persson, J. W. Andreasen, W. Thiel, M. Berggren, X. Crispin, D. Fazzi and S. Fabiano, *Adv Mater*, 2016, **28**, 10764-+.
113. R. A. Schlitz, F. G. Brunetti, A. M. Glaudell, P. L. Miller, M. A. Brady, C. J. Takacs, C. J. Hawker and M. L. Chabinyc, *Adv Mater*, 2014, **26**, 2825-2830.
114. M. Stoppa and A. Chiolerio, *Sensors-Basel*, 2014, **14**, 11957-11992.
115. S. Takamatsu, T. Lonjaret, D. Crisp, J. M. Badier, G. G. Malliaras and E. Ismailova, *Sci Rep-Uk*, 2015, **5**.

116. J. A. Lee, M. K. Shin, S. H. Kim, H. U. Cho, G. M. Spinks, G. G. Wallace, M. D. Lima, X. Lepro, M. E. Kozlov, R. H. Baughman and S. J. Kim, *Nat Commun*, 2013, **4**.
117. W. Weng, P. N. Chen, S. S. He, X. M. Sun and H. S. Peng, *Angew Chem Int Edit*, 2016, **55**, 6140-6169.
118. X. Pu, L. X. Li, M. M. Liu, C. Y. Jiang, C. H. Du, Z. F. Zhao, W. G. Hu and Z. L. Wang, *Adv Mater*, 2016, **28**, 98-+.
119. K. Jost, G. Dion and Y. Gogotsi, *J Mater Chem A*, 2014, **2**, 10776-10787.
120. J. Chen, Y. Huang, N. N. Zhang, H. Y. Zou, R. Y. Liu, C. Y. Tao, X. Fan and Z. L. Wang, *Nat Energy*, 2016, **1**.
121. F. C. Krebs, M. Biancardo, B. Winther-Jensen, H. Spanggard and J. Alstrup, *Sol Energ Mat Sol C*, 2006, **90**, 1058-1067.
122. N. N. Zhang, J. Chen, Y. Huang, W. W. Guo, J. Yang, J. Du, X. Fan and C. Y. Tao, *Adv Mater*, 2016, **28**, 263-269.
123. N. Soin, T. H. Shah, S. C. Anand, J. F. Geng, W. Pornwannachai, P. Mandal, D. Reid, S. Sharma, R. L. Hadimani, D. V. Bayramol and E. Siores, *Energ Environ Sci*, 2014, **7**, 1670-1679.
124. A. Lund, K. Rundqvist, E. Nilsson, L. Yu, B. Hagström and C. Müller, *npj Flexible Electronics*, 2018, **2**, 9.
125. L. M. Liu, J. Pan, P. N. Chen, J. Zhang, X. H. Yu, X. Ding, B. J. Wang, X. M. Sun and H. S. Peng, *J Mater Chem A*, 2016, **4**, 6077-6083.
126. J. A. Lee, A. E. Aliev, J. S. Bykova, M. J. de Andrade, D. Kim, H. J. Sim, X. Lepro, A. A. Zakhidov, J. B. Lee, G. M. Spinks, S. Roth, S. J. Kim and R. H. Baughman, *Adv Mater*, 2016, **28**, 5038-5044.
127. S. J. Kim, J. H. We and B. J. Cho, *Energ Environ Sci*, 2014, **7**, 1959-1965.
128. J. P. O'Brien, S. R. Fahnestock, Y. Termonia and K. C. H. Gardner, *Adv Mater*, 1998, **10**, 1185-+.
129. J. B. Quig, *Text Res J*, 1953, **23**, 280-288.
130. V. B. Gupta and V. K. Kothari, *Manufactured Fibre Technology*, Chapman and Hall, London, 1997,
131. Y. Cao, P. Smith and A. J. Heeger, *Polymer*, 1991, **32**, 1210-1218.
132. J. Zhou, E. Q. Li, R. P. Li, X. Z. Xu, I. A. Ventura, A. Moussawi, D. H. Anjum, M. N. Hedhili, D. M. Smilgies, G. Lubineau and S. T. Thoroddsen, *J Mater Chem C*, 2015, **3**, 2528-2538.
133. D. Esrafilzadeh, R. Jalili, E. M. Stewart, S. H. Aboutalebi, J. M. Razal, S. E. Moulton and G. G. Wallace, *Adv Funct Mater*, 2016, **26**, 3105-3117.
134. C. Müller and O. Inganäs, *Bio-Based Materials as Templates for Electronic Devices*, John Wiley and Sons, Germany, 2012,
135. Z. S. Lu, C. P. Mao and H. H. Zhang, *J Mater Chem C*, 2015, **3**, 4265-4268.
136. R. H. Karlsson, A. Herland, M. Hamedi, J. A. Wigenius, A. Aslund, X. J. Liu, M. Fahlman, O. Inganas and P. Konradsson, *Chem Mater*, 2009, **21**, 1815-1821.

137. A. Matsumoto, J. Chen, A. L. Collette, U. J. Kim, G. H. Altman, P. Cebe and D. L. Kaplan, *J Phys Chem B*, 2006, **110**, 21630-21638.
138. H. Wang, U. Ail, R. Gabrielsson, M. Berggren and X. Crispin, *Adv Energy Mater*, 2015, **5**.
139. C. Muller, R. Jansson, A. Elfwing, G. Askarieh, R. Karlsson, M. Hamedi, A. Rising, J. Johansson, O. Inganas and M. Hedhammar, *J Mater Chem*, 2011, **21**, 2909-2915.
140. E. Steven, W. R. Saleh, V. Lebedev, S. F. A. Acquah, V. Laukhin, R. G. Alamo and J. S. Brooks, *Nat Commun*, 2013, **4**.
141. A. Hakansson, S. B. Han, S. H. Wang, J. Lu, S. Braun, M. Fahlman, M. Berggren, X. Crispin and S. Fabiano, *J Polym Sci Pol Phys*, 2017, **55**, 814-820.
142. J. D. Ryan, A. Lund, A. I. Hofmann, R. Kroon, R. Sarabia-Riquelme, M. C. Weisenberger and C. Müller, *Manuscript*, est. 2018
143. M. K. Chun, C. S. Cho and H. K. Choi, *J Control Release*, 2002, **81**, 327-334.
144. J. F. Yaung and T. K. Kwei, *J Appl Polym Sci*, 1998, **69**, 921-930.